Towards personalized computer simulation of breast cancer treatment: a multi-scale pharmacokinetic and pharmacodynamic model informed by multi-type patient data

Supplementary Material

Xiaoran Lai[1], Oliver M Geier[2], Thomas Fleischer[3], Øystein Garred[4], Elin Borgen[4], Simon Wolfgang Funke[5], Surendra Kumar[3], Marie Elisabeth Rognes[5], Therese Seierstad[6], Anne-Lise Børresen-Dale[3], Vessela N. Kristensen[3,7,8], Olav Engebraaten[9,10], Alvaro Köhn-Luque[1,*] and Arnoldo Frigessi[1,11,*]

[1]Oslo Centre for Biostatistics and Epidemiology, Faculty of Medicine, University of Oslo
[2]Department of Diagnostic Physics, Clinic of Radiology and Nuclear Medicine, Oslo University Hospital
[3]Department of Genetics, Institute for Cancer Research, Oslo University Hospital
[4]Department of Pathology, Oslo University Hospital
[5]Center for Biomedical Computing, Simula Research Laboratory, Oslo
[6]Department of Radiology and Nuclear Medicine, Oslo University Hospital
[7]Department of Clinical Molecular Biology and Laboratory Science (EpiGen), Akershus University Hospital, Division of Medicine, Lørenskog, Norway
[8]Institute of Clinical Medicine, Falculty of Medicine, University of Oslo, Oslo, Norway
[9]Department of Oncology, Oslo University Hospital
[10]Department of Tumor Biology, Institute for Cancer Research, University of Oslo
[11]Oslo Centre for Biostatistics and Epidemiology, Oslo University Hospital
*Joint last authors

May 14, 2019

Contents

S1   Clinical data set

Here we present the clinical data set used to inform our mathematical model. An overview of the available data for each patient is shown in table S1 and additional images and information are displayed below.

Patient ID		1	2	3	4
Number of histopathology images		2	2	2	2
DCE-MRI	week 0	✓	✓	✓	✓
DW-MRI	week 1	✓	-	✓	✓
	week12	-	✓	✓	✓
PAM50 subtype		Luminal B	Basal	HER2	Basal
Proliferation score		0.5055	2.3730	2.1349	2.2035
VEGF expression		0.1834	0.6449	2.32	1.38
TP53 expression		0.1475	0.8504	-0.78	-0.02
TP53 Status		wild-type	wild-type	wild-type	mutated
HIF-α pathway score	week 0	0.7620846	0.8311913	1	0.8913964
	week 12	0.6298112	-	0.8981043	0.1990078

Table S1: Clinical data overview.

S1.1 Inclusion criteria

Patients with HER2-negative mammary carcinomas with size ≥ 2.5 cm previously untreated for breast cancer were eligible. Other key inclusion criteria were WHO performance status ≤ 2, adequate hematologic and biochemical parameters, no sign of metastatic disease and normal organ function in general. Before surgery, the patients were treated with chemotherapy before surgery (FEC100, 4 courses during 12 weeks, thereafter taxane treatment - docetaxel or paclitaxel -, and randomized 1:1 to receive bevacizumab, 15 mg/kg every third week given concurrently with chemotherapy, or 10 mg/kg every other week with weekly paclitaxel administration.

Patients were recruited at two sites in Norway (Oslo University Hospital, Oslo and St. Olav's Hospital, Trondheim), between 2008 and 2012. Written informed consent was obtained from all patients prior to inclusion. The study was approved by the Institutional Protocol Review Board, the regional ethics committee, the Norwegian Medicines Agency, and carried out in accordance with the Declaration of Helsinki, International Conference on Harmony/Good Clinical practice. The study is registered in the http://www.ClinicalTrials.gov/ database with the identifier NCT00773695.

S1.2 Histopathology

The histopathological analysis was performed on needle biopsies taken from the breast tumors at week 0. The tissue was fixed in formalin, embedded in paraffin and hematoxylin-eosin-stained (H&E) sections were prepared. For each patient, two images of the histopathological slides, biopsy A and B, at 20x magnification were used, see figs. S1 and S4. The physical size of a pixel in the digital images (0.148 μm) was calculated using nano-beads with 4 μm diameters at the same resolution as the histological images.
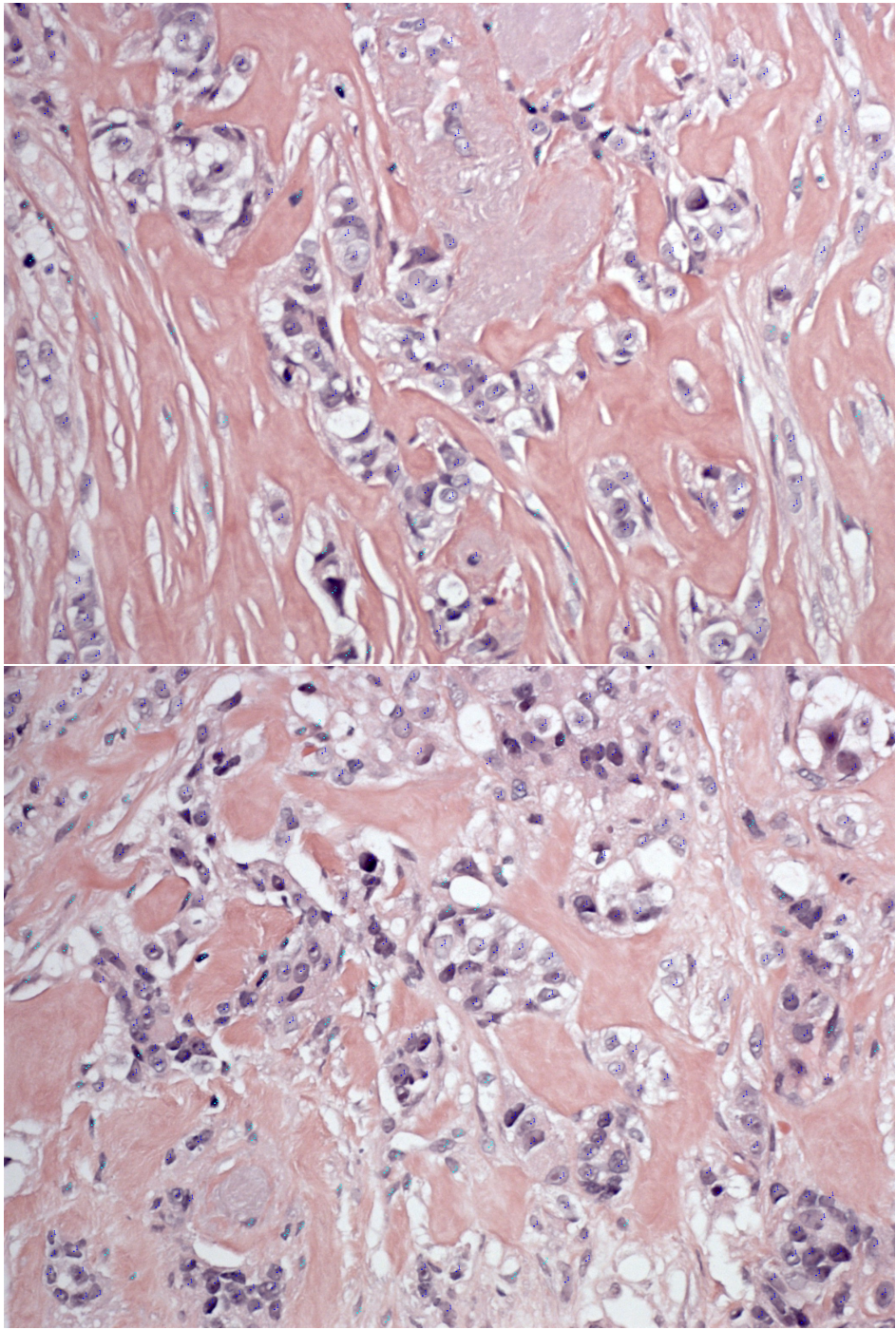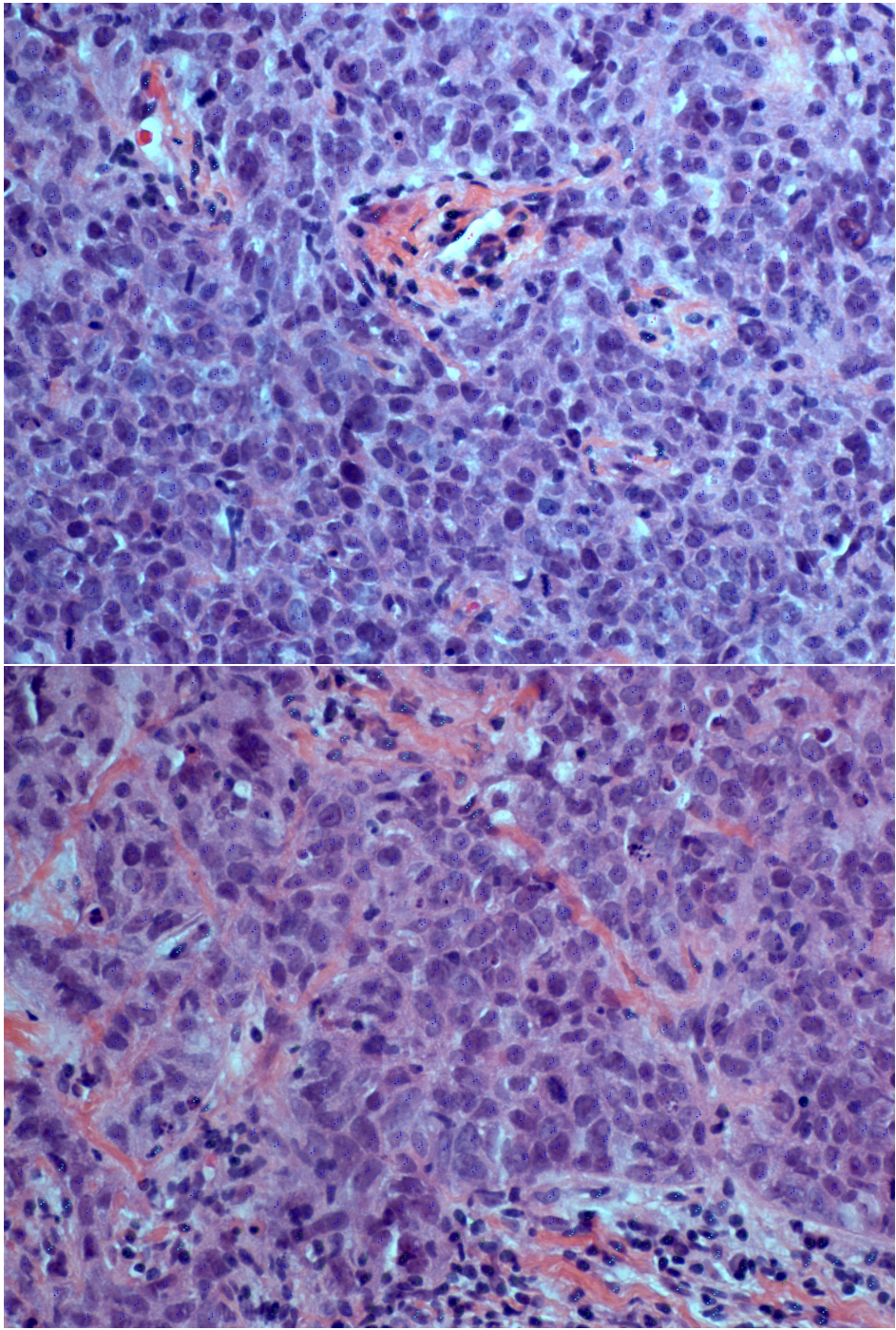
Figure S1: Biopsy A and B of patient 1

Figure S2: Biopsy images A and B of patient 2
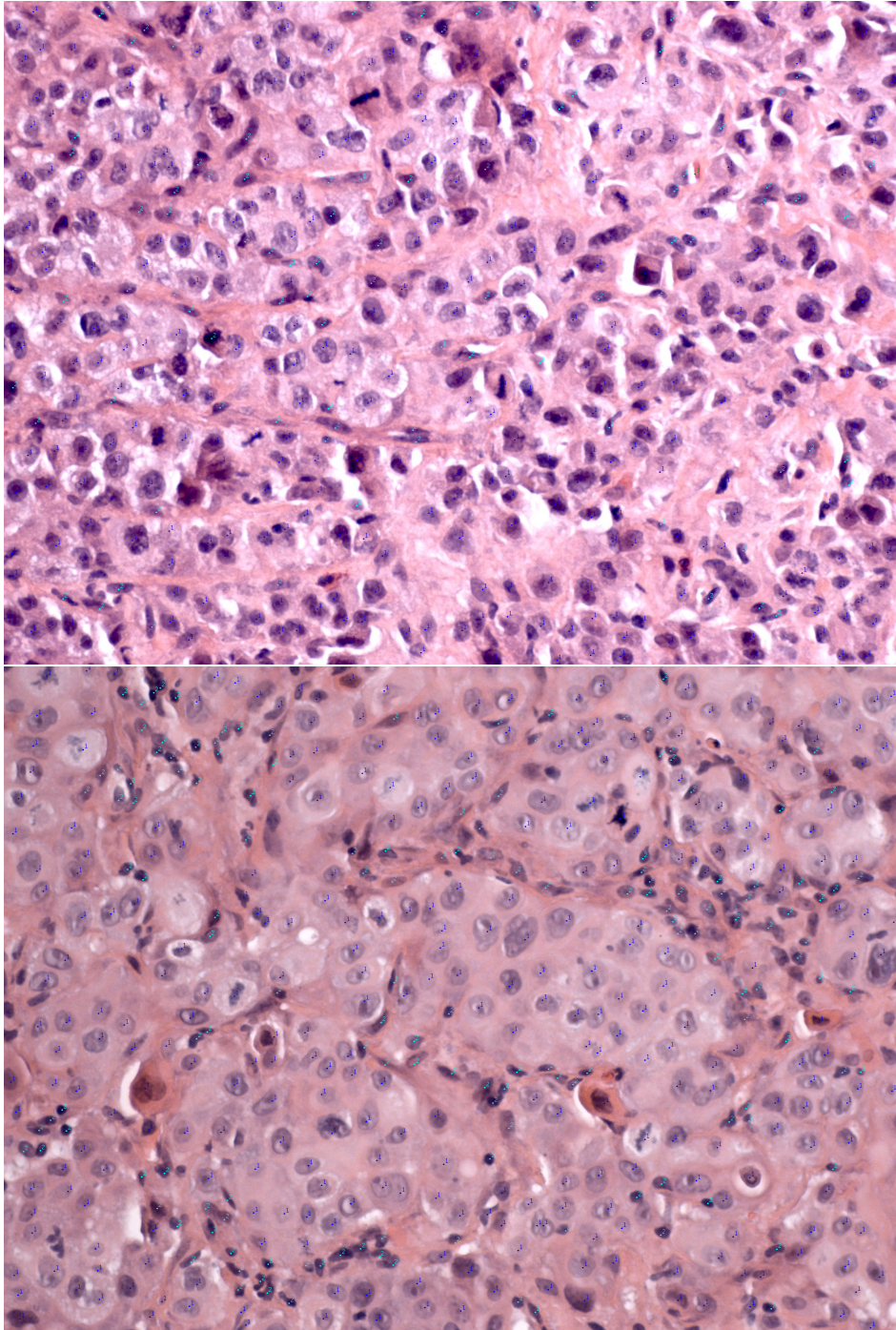
Figure S3: Biopsy images A and B of patient 3
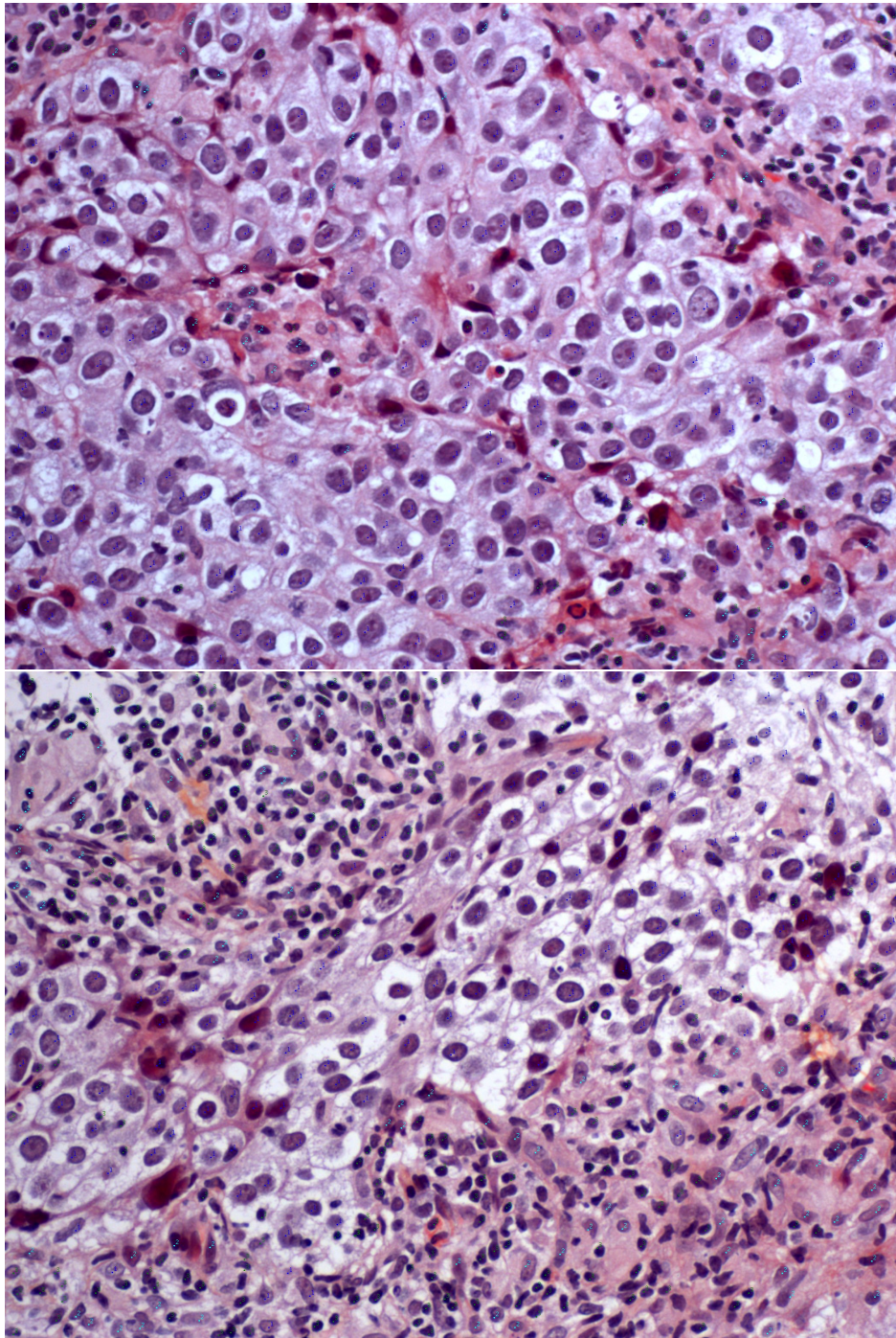
Figure S4: Biopsy images A and B of patient 4

S1.3 Magnetic Resonance Imaging

In addition to morphological MR images (sagittal T1-weighted, axial T2-weighted), the imaging protocol included a radial 3D T1-weighted spoiled gradient dynamic contrast-enhanced

(DCE-MRI) with k-space weighted image contrast [27] and diffusion weighted (DW-MRI) using five different b-values (0, 50, 100, 250 and 800 s/mm^2) [26]. For DCE-MRI, Gadovist (Bayer, Pharma, Germany, 0.08 mmol/kg body weight) was administered intravenously with a power injector followed by a 20 mL saline flush. Forty consecutive image series including eight precontrast series, were acquired with a time resolution of 13 seconds [27]. Image analysis was performed using nICE (Nordic NeuroLab, Bergen, Norway). For DCE-MRI analysis, an extended Tofts model was used, which included the determination of the contrast-enhancement curve of the contrast agent in each individual voxel (volume $1\,\text{mm} \times 1\,\text{mm} \times 1.5\,\text{mm}$). For this purpose pre-contrast relaxation times T10 of blood from reference [9] and breast tissues from reference [38] were used. As shown in [27], for a time resolution of 13 seconds, the relative error of parameter k_{trans} is within 10 % of normal values. However, for parameter v_p a resolution of 8 seconds is required and the obtained values could be over-estimated [8]. DWI data were analyzed using a simplified IVIM model-based analysis as described in [3]. Below we show MRI data for each patient in a section of the breast where the tumor is visible. In fig. S9we also show the apparent diffusion coefficient (ADC) within segmented tumor region estimated from DW-MR data.
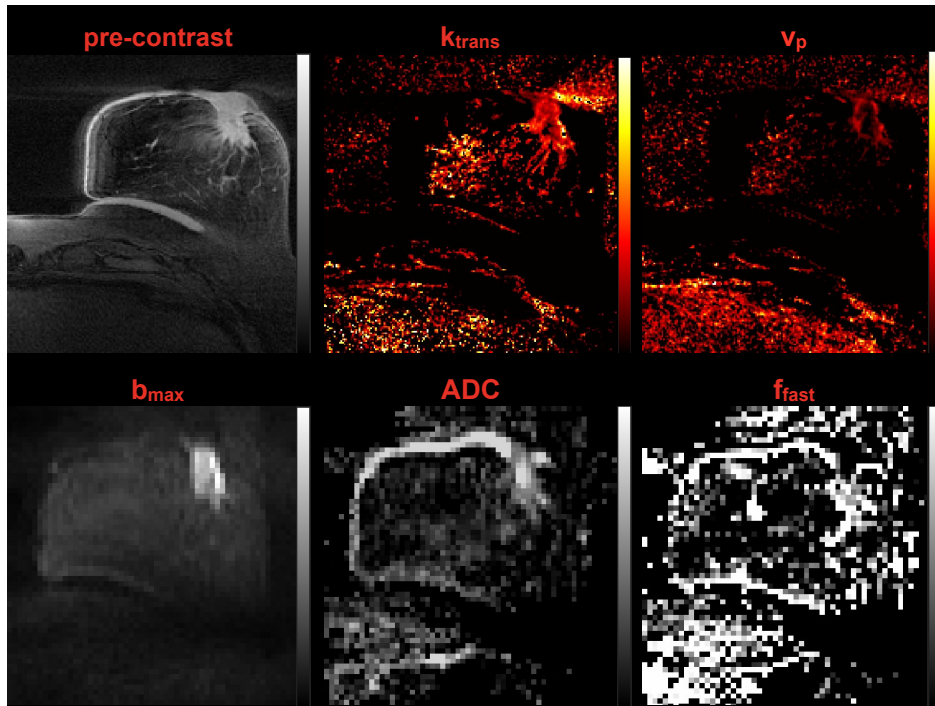
Figure S5: MR images of patient 1 at week 0
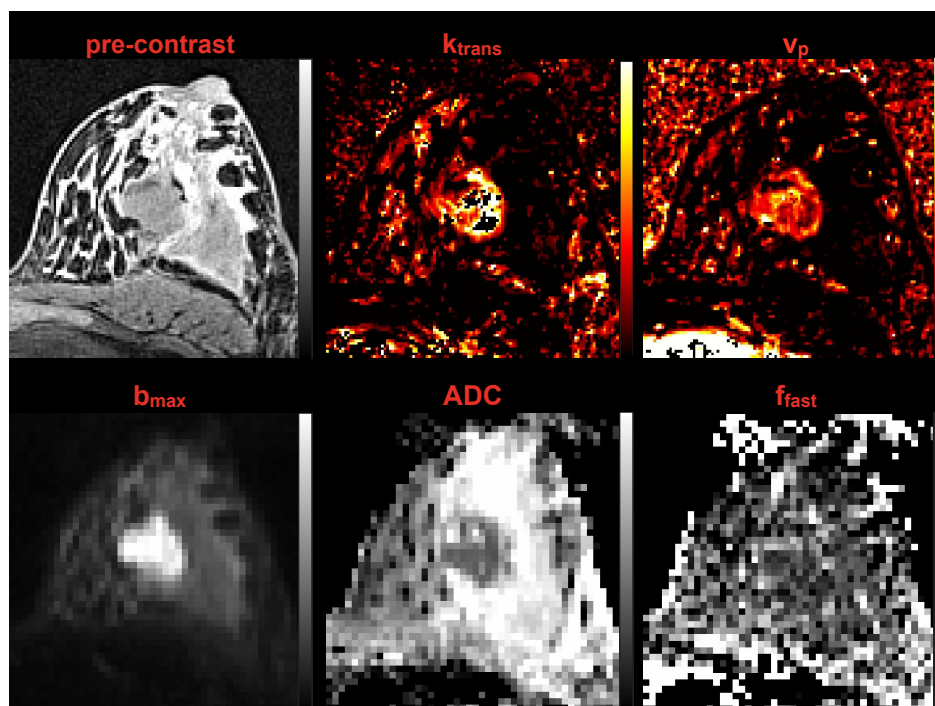
Figure S6: MR images of patient 2 at week 0
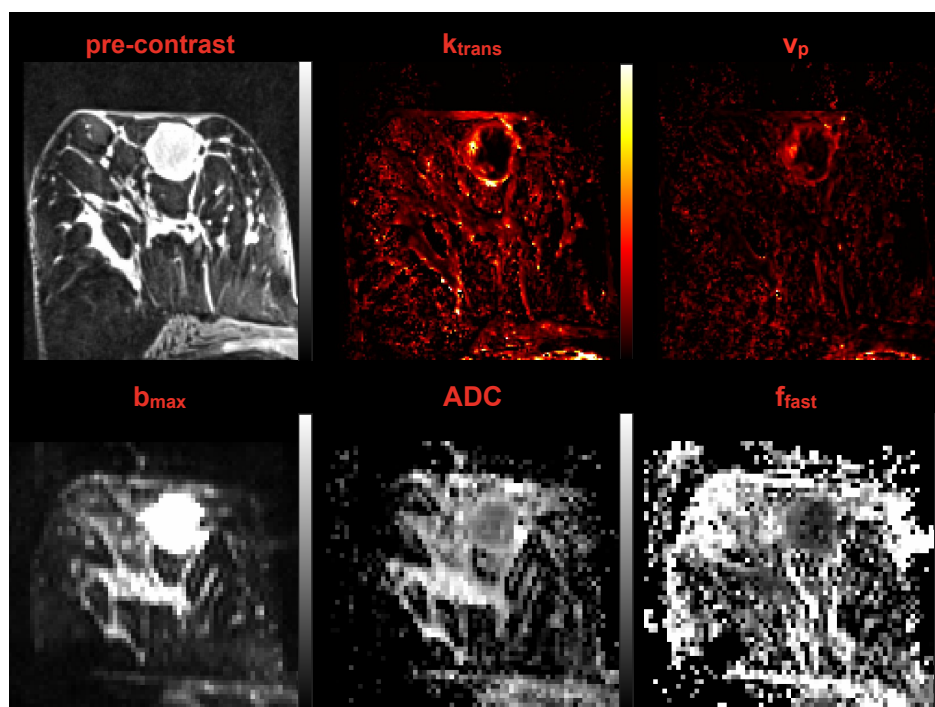
Figure S7: MR images of patient 3 at week 0
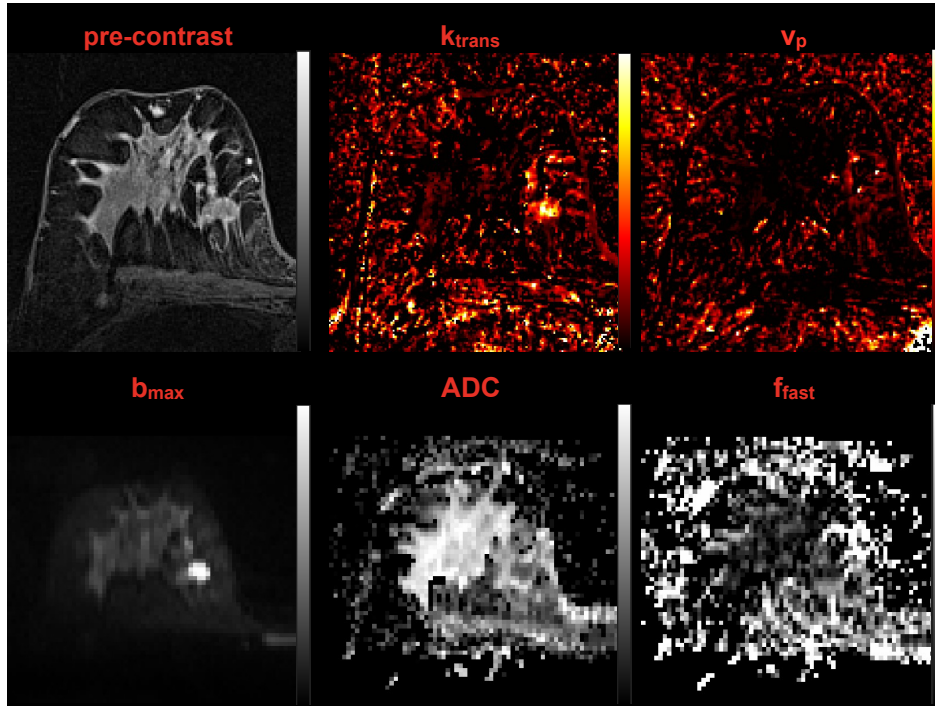
Figure S8: MR images of patient 3 at week 0

(a) Patient 1

(b) Patient 2

(c) Patient 3
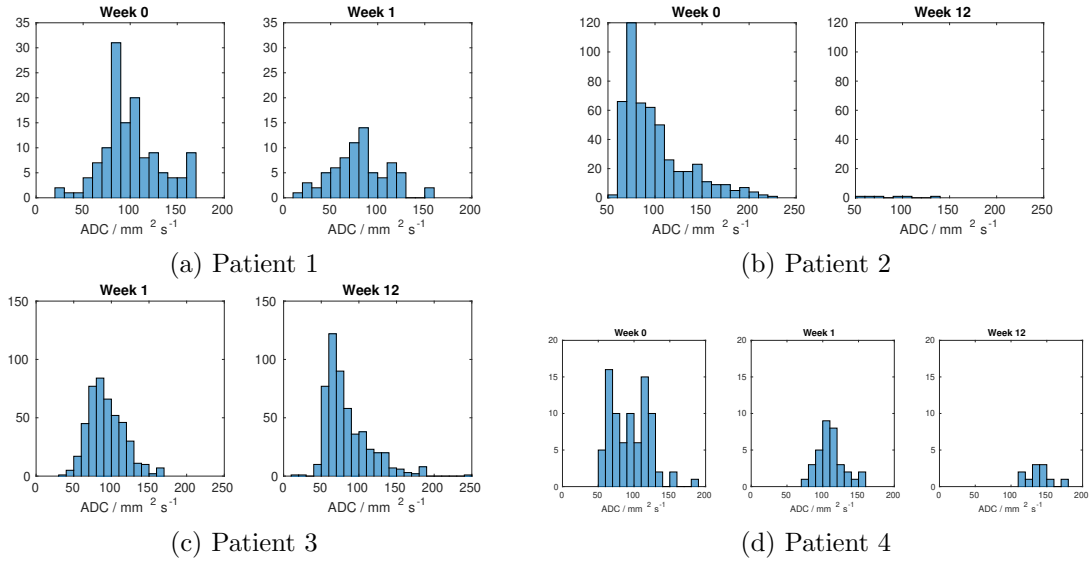
(d) Patient 4

Figure S9: Apparent Diffusion Coefficient (ADC) of all four patients at different time points.

S1.4 Molecular data

Here we show molecular data of the four patients. The density of all 143 patients at screening in the NeoAva cohort is also shown for comparison. In fig. S10d, four patients were compared

against 50 tumor-free control.

(a) VEGF mRNA expression of all patients in the trial ($n = 143$) at screening

(b) TP53 mRNA expression of all patients in the trial ($n = 143$) at screening

(c) Proliferation score of all patients in the trial ($n = 143$) at screening

(d) HIF-α pathway score of four patients compared to control of tumor-free tissue ($n = 50$) at screening and week 12
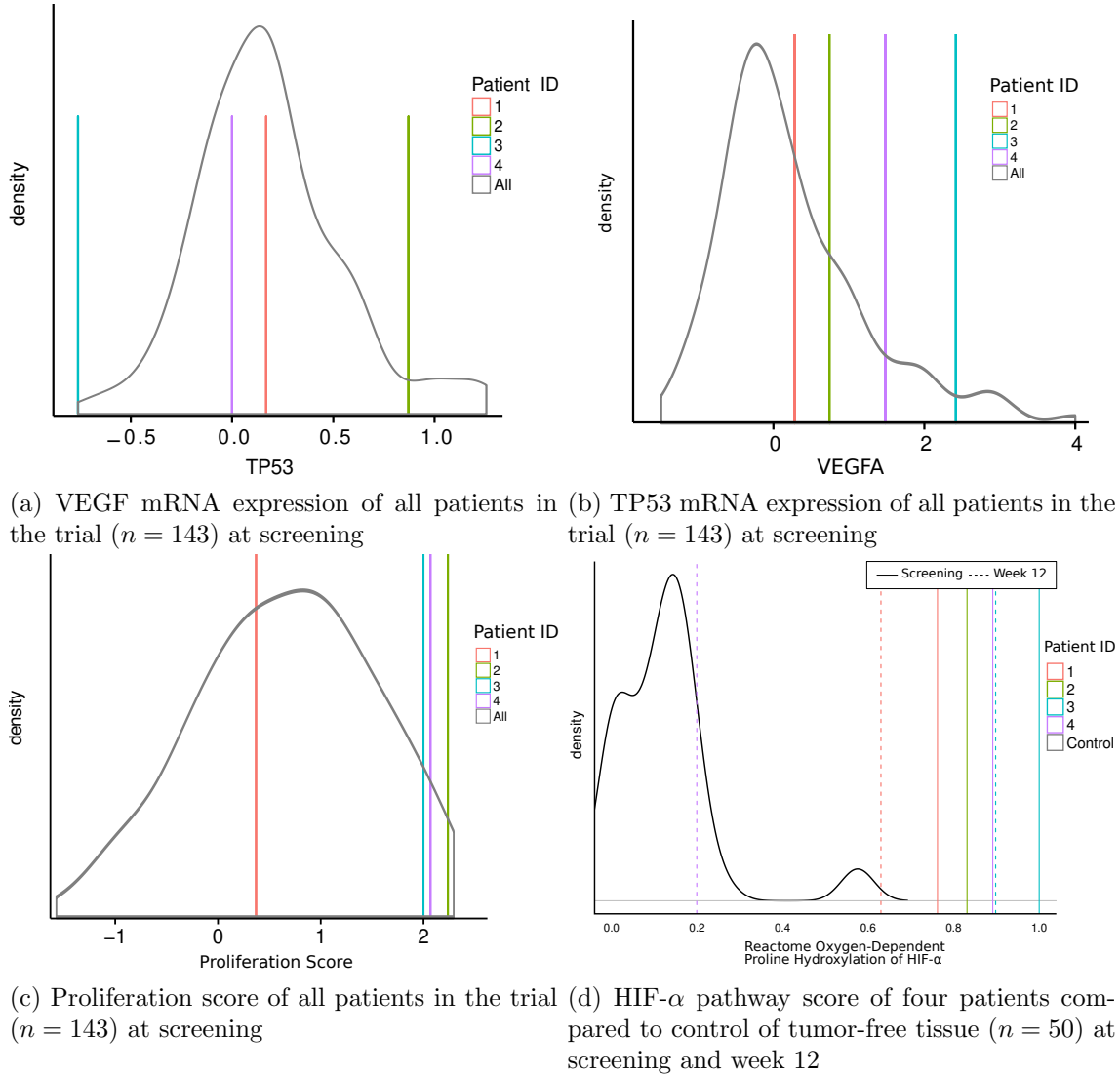
Figure S10: Molecular data used from the study

S2 Multi-scale mathematical model

This section describes in full detail the multi-scale pharmacokinetic and pharmacodynamic model used in this study. We model the response of a cross section of tumor tissue to a combination of chemotherapeutic and anti-angiogenic agents using a hybrid cellular automaton [1, 32]. Thus, a tumor section is represented by a finite regular square lattice L, consisting of a set of nodes labeled by their positions $\boldsymbol{x} \in L, \boldsymbol{x} = (i\Delta x, j\Delta x), i = 0, .., n - 1, j = 0, ..., m - 1$, being Δx the distance between nearest nodes. Biological cells and cross-sectional cuts of functional tumor vessels are modeled as individual agents occupying a single lattice node.

Microenvironmental factors in the tissue section, such as oxygen are modeled as continuous variables over domain $D = [0, (n-1)\Delta x] \times [0, (m-1)\Delta x] \subset \mathbb{R}^2$. Intracellular and intravascular processes are modeled as continuous variables associated to each cell and blood vessel, respectively. To account for cell and blood vessel dynamics and the molecular factors that control them we build five interlinked model modules: cellular, subcellular, extracellular, vascular and intravascular modules. Figure S11 shows a diagram with the main components of each module and the interactions between them. A detailed description of each module is provided below.
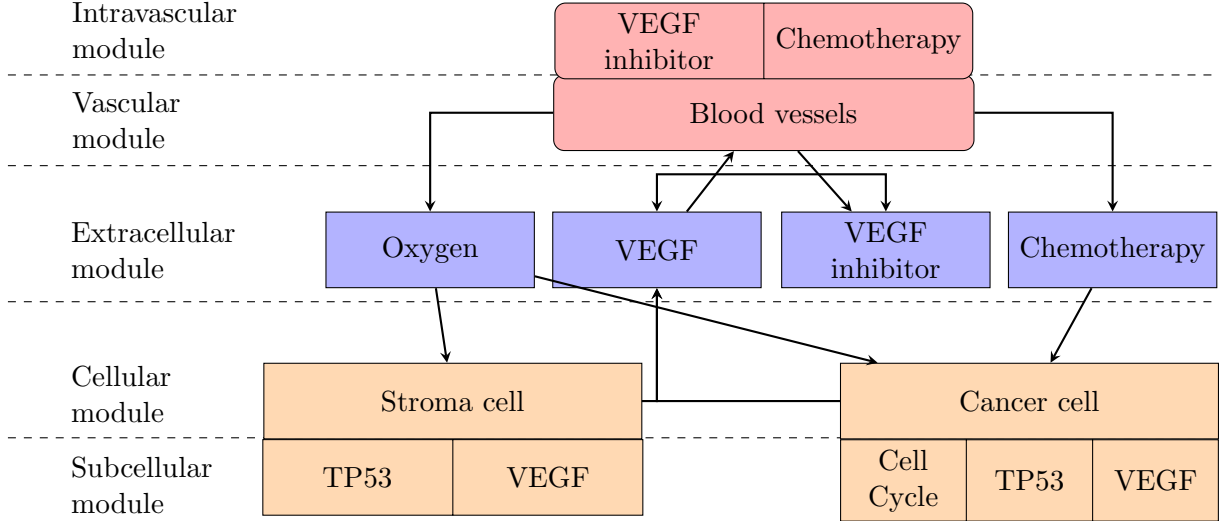
Figure S11: Modular structure of the hybrid cellular automaton model for vascular tumor growth and combination therapy. The main components of each module are displayed. Direction of arrows indicate influence between different components.

S2.1   Cellular module

The presence of cancer and stroma cells on the lattice sites at time t, is given by a function $\mathcal{L}$ that takes three possible values: $\mathcal{L}(\boldsymbol{x}, t) = 0$ (if the site $\boldsymbol{x}$ is empty), $\mathcal{L}(\boldsymbol{x}, t) = 1$, (if $\boldsymbol{x}$ is occupied by a cancer cell) or $\mathcal{L}(\boldsymbol{x}, t) = 2$ (if $\boldsymbol{x}$ is occupied by a stroma cell). To account for physical space restrictions in the tissue, at most one cell can occupy one site of the grid. We assume that cancer cells can divide or die, while stroma cells cannot do either. This is based on cancer cells proliferate much more than normal cells and that the employed anthracycline drugs can only kill proliferating cells [39]. We could introduce a birth and death dynamics also for stroma cells, however, in the current version of the model, this is simplified to a static situation as several parameters related to this process need to be specified. Cell migration and cell movements due to mechanical deformations are also neglected.

S2.1.1 Cancer cells

Cancer cell division is controlled by an internal cell cycle clock described in the subcellular module below. When a cell has passed the checkpoint G_1/S and it is committed to divide, it can be killed by the FEC chemotherapeutic agents [39]. We model the probability for a cell to be killed by FEC at a certain dose with a beta distribution $Beta(\alpha, \beta)$. For $\alpha = 1$, this distribution approximates FEC dose-response data obtained from *in vitro* cultures of breast cancer cells derived from 140 chemotherapy-naïve patients at the time of primary surgery [15]. That means the concentration of each FEC agent, expressed as percentage of peak plasma concentration (% PPC), at the cell location, and parameter β determine the probability of cell killing given by value of the $Beta(1, \beta)$ distribution function at a given %PPC. If the cell dies, it is removed from the computational grid. If chemotherapy does not kill the proliferating cell, a daughter cell is placed at an empty neighbor location with the highest oxygen concentration. If, however, no free space is available in the neighborhood, the cell cycle of the parent cell is reset to zero and no daughter cell is produced. In this way we represent physical space constraints.

S2.1.2 Stroma cells

As stroma cells in our cellular automaton do not proliferate or die, their role in the model is restricted to space and oxygen competition with cancer cells and production of VEGF under hypoxia. We also neglect other roles that stroma cells have in influencing treatment outcome, such as possible hindrance or cooperation with tumor cells.

S2.2 Vascular module

We assume that blood vessels are perpendicular to the tumor section and for simplicity we consider they all have the same size. The presence of cross-sectional cuts of functional tumor vessels in the lattice at time t is given by function $\mathcal{G}$, with $\mathcal{G}(\boldsymbol{x}, t) = 1$ representing the presence of a functional vessel, and $\mathcal{G}(\boldsymbol{x}, t) = 0$ otherwise. Vessel dynamics is modeled by a birth-death process, with the probability of creating and removing vessels depending on the spatial distribution of extracellular VEGF. Specifically, we assume that a functional vessel can be created with certain probability if the amount of VEGF is within a specified range. If the amount of VEGF is too high, endothelial cells can be highly proliferative and migratory [36] thus making the vessel non-functional, i.e, rendering them incapable of transferring oxygen and other nutrients [29]. If VEGF is too low, vessels can disappear as a result of pruning [10]. Thus, in every time interval $[t, t + \Delta v]$, we define the probability of creating and removing a vessel at $\boldsymbol{x} \in G$ as:

$$P(\mathcal{G}(\boldsymbol{x}, t + \Delta v) = 1 \mid \mathcal{G}(\boldsymbol{x}, t) = 0) = p_{\text{birth}} \quad \text{if} \quad \text{Low}_V < V(\boldsymbol{x}, t) < \text{High}_V$$
$$P(\mathcal{G}(\boldsymbol{x}, t + \Delta v) = 0 \mid \mathcal{G}(\boldsymbol{x}, t) = 1) = p_{\text{death}} \quad \text{if} \quad V(\boldsymbol{x}, t) < \text{Low}_V \quad \text{or} \quad V(\boldsymbol{x}, t) > \text{High}_V$$
$$\text{(S1)}$$

where Low_V and High_V are the lower and upper thresholds of the VEGF range where vessels are viable, and $V(\boldsymbol{x}, t)$ denotes the extracellular concentration of VEGF at location $\boldsymbol{x}$ at time t. The dynamic of $V(\boldsymbol{x}, t)$ is described in section S2.4.2 below. If a vessel at location $\boldsymbol{x}$ and time t is functional, it will continue to be so whenever $\text{Low}_V < V(\boldsymbol{x}, t) < \text{High}_V$. Note

that the probabilities p_{birth} and p_{death} model the influence of vessel creation and removal depending on the VEGF concentration. For instance, if p_{death} is low, vessels could remain even if VEGF is outside the viable range.

S2.3 Subcellular module

In this module we consider two subcellular processes that are the target of chemotherapeutic and anti-angiogenic drugs and are therefore key to describe their action on the tumor section, namely the cell cycle and TP53-VEGF signaling. Following [1, 28], we model them using a system of three ordinary differential equations associated to each living cell.

S2.3.1 Cell-cycle

To consider the cell-cycle in each cancer cell, we use a simple phase model proposed in [28]. It describes the speed of the progress through the cell cycle as a function of the oxygen concentration at the cell location using the ordinary differential equation:

$$\frac{d\phi_{\boldsymbol{x}}}{dt} = \frac{K(\boldsymbol{x}, t)}{T_{\min}(K_\phi + K(\boldsymbol{x}, t))}. \tag{S2}$$

where $\phi_{\boldsymbol{x}}(t) \in \mathbb{R}^+$ represents an internal state of the cell in location $\boldsymbol{x} \in L$ at time t. We assume that the cell cycle starts at $\phi = 0$ and when $\phi \geq 1$, the cell has passed the check point G_1/S and it is committed to divide. If the cell is not killed by the chemotherapy and succeeds to divide, the state is reset to zero. $K(\boldsymbol{x}, t)$ is the oxygen concentration at time t in the position $\boldsymbol{x} \in L$ where the cell is located. Parameter $T_{\min}$ is the minimum period of the cell cycle (in oxygen rich conditions) and K_ϕ is the oxygen concentration at which the speed is half-maximal. To account for stochastic variability in cell cycle length, at each cell division the $T_{\min}$ of the daughter cell is drawn from a normal distribution $\mathcal{N}(T_{min}, 1)$.

S2.3.2 TP53-VEGF signaling

Following references [1, 28], we assume that hypoxia upregulates the intracellular levels of TP53 and VEGF. More precisely, we assume that the background production rates of TP53 and VEGF are constant and that their decay rates are modulated by the local level of extracellular oxygen following Michaelis-Mente kinetics. Moreover, while in wild-type *TP53* cells, TP53 inhibits VEGF production, in cancer cells with mutated *TP53*, TP53 increases VEGF production [33]. The dynamics of TP53 and VEGF, denoted by $[\text{TP53}]_{\boldsymbol{x}} = [\text{TP53}]_{\boldsymbol{x}}(t)$ and $[\text{sVEGF}]_{\boldsymbol{x}} = [\text{sVEGF}]_{\boldsymbol{x}}(t), \boldsymbol{x} \in L$ respectively, are then coupled to one-another, and to the extracellular oxygen concentration, as described by the following system of differential equations:

$$\frac{d[\text{TP53}]_{\boldsymbol{x}}}{dt} = k_7 - k_7' \frac{K(\boldsymbol{x}, t)}{K_{\text{TP53}} + K(\boldsymbol{x}, t)}[\text{TP53}]_{\boldsymbol{x}}, \tag{S3}$$

$$\frac{d[\text{sVEGF}]_{\boldsymbol{x}}}{dt} = k_8 - k_8' \frac{K(\boldsymbol{x}, t)}{K_{\text{VEGF}} + K(\boldsymbol{x}, t)}[\text{sVEGF}]_{\boldsymbol{x}} + k_8'' \frac{[\text{TP53}]_{\boldsymbol{x}}[\text{sVEGF}]_{\boldsymbol{x}}}{J_5 + [\text{sVEGF}]_{\boldsymbol{x}}}, \tag{S4}$$

14

where k_7 is the basal rate of TP53 synthesis, k_7' is the maximal degradation rate of TP53 by oxygen and K_{TP53} is the oxygen concentration at which the rate is half-maximal. Parameter k_8 is a basal rate of VEGF production and k_8' is the maximal rate of VEGF inhibitory production by oxygen, accounting for stimulation of VEGF expression by hypoxia. Parameter K_{VEGF} is the oxygen concentration at which the rate is half-maximal. Parameter k_8'' represents the maximal rate effect in VEGF production by TP53, which is assumed to be negative in wild-type *TP53* cells, and positive for mutated *TP53*. Parameter J_5 is the intracellular VEGF concentration when intracellular VEGF production is half maximal.

S2.4   Extracellular module

The extracellular module accounts for the dynamics of diffusible molecules of interest, namely oxygen, VEGF and the drugs used in the clinical study. We model their spatio-temporal concentrations using reaction-diffusion equations and solve them over the whole domain D by imposing no-flux boundary conditions along the edges of the domain.

S2.4.1   Oxygen concentration

We model oxygen diffusion in the tumor tissue, oxygen supply by blood vessels and oxygen consumption by cells as follows. Find oxygen concentration $K = K(x, t)$ satisfying:

$$s_K \frac{\partial K}{dt} - D_k \nabla^2 K = r_k(K_0 - K)\mathcal{G}(\boldsymbol{x}, t) - \frac{\phi_k K}{K_1 + K}\delta(\boldsymbol{x}, t), \tag{S5}$$

where $S_K \in \{0, 1\}$, and

$$\delta(\boldsymbol{x}, t) = \begin{cases} 0 & \text{if} \quad \mathcal{L}(\boldsymbol{x}, t) = 0 & \text{(no cell)} \\ 1 & \text{if} \quad \mathcal{L}(\boldsymbol{x}, t) = 1, 2 & \text{(cell present)}, \end{cases}$$

D_k is the diffusion coefficient of oxygen in the tumor tissue, r_k is the supply rate of oxygen by blood vessels, also called surface-permeability product. We call K_0 the oxygen concentration inside the tumor vasculature assumed to be constant. Oxygen consumption is modeled in eq. (S5) by a Michaelis-Mente term that accounts for an almost constant consumption rate for high oxygen concentration, followed by a rapid decrease as the oxygen concentration decreases [5]. Parameter ϕ_k is the maximal consumption rate in oxygen rich conditions, and K_1 is the oxygen concentration for which oxygen consumption is half maximal.

S2.4.2   VEGF concentration

We model VEGF diffusion in the tumor tissue, production by cells, binding and unbinding to the VEGF-inhibitor and decay as follows. Find VEGF concentration $V = V(x, t)$ satisfying:

$$s_V \cdot \frac{\partial V}{dt} - D_v \nabla^2 V = r_v([\text{sVEGF}]_{\boldsymbol{x}})\delta(\boldsymbol{x}, t) + k_d C - k_a A_e V - \psi_v V, \tag{S6}$$

where D_v is the diffusion coefficient, the function r_v represents VEGF secretion rate by cells which we assume to be a linear function of the VEGF expression in each cell, *i.e.*, $r_v([\text{sVEGF}]_{\boldsymbol{x}}) = a[\text{sVEGF}]_{\boldsymbol{x}} + b$. Parameters k_d and k_a are the dissociation and association rates to the VEGF-inhibitor and ψ_v is the decay rate.

15

S2.4.3 VEGF-inhibitor concentration

The VEGF-inhibitor bevacizumab reversibly binds VEGF and prevents the interaction of VEGF to its receptors (Flt-1 and KDR) on the surface of endothelial cells. We model diffusion, supply by blood vessels, binding and unbinding to VEGF, as follows. Find VEGF-inhibitor concentration $A = A(x, t)$ satisfying:

$$s_A \cdot \frac{\partial A}{dt} - D_A \nabla^2 A = r_A(A_1(t) - A)\mathcal{G}(\boldsymbol{x}, t) + k_d C - k_a AV, \tag{S7}$$

where D_A is the diffusion coefficient, r_A is the supply rate by blood vessels (or permeability surface product) and ψ_A is the decay rate in the tumor tissue. The time evolution of the VEGF-inhibitor concentration in plasma, A_1, is described in the intravascular module below. Parameters k_d and k_a were introduced above.

S2.4.4 VEGF/VEGF-inhibitor complex concentration

We model diffusion in the tumor tissue, binding, unbinding and decay as follows. Find VEGF/VEGF inhibitor complex $C = C(x, t)$ satisfying:

$$s_C \cdot \frac{\partial C}{dt} - D_C \nabla^2 C = k_a AV - k_d C - \psi_C C, \tag{S8}$$

where D_C is the diffusion coefficient and ψ_C is the decay rate in the tumor tissue. Parameters k_d and k_a were introduced above.

S2.4.5 Chemotherapy concentrations

For each chemotherapeutic drug $j = 1, 2, 3$, we model diffusion in the tumor tissue, supply and clearance by blood and vessels as follows. Find chemotherapy concentration $G^j = G^j(x, t)$ satisfying:

$$\frac{\partial G^j}{dt} - D_{G^j} \nabla^2 G^j = r_{G^j}(G_1^j(t) - G^j)\mathcal{G}(\boldsymbol{x}, t) - \psi_{G^j} G^j \tag{S9}$$

where D_{G^j} is the diffusion coefficient, r_{G^j} is the supply rate by vessels (or permeability surface product) and ψ_{G^j} represents a removal rate that accounts for drug uptake and decay.

S2.5 Intravascular module

The time evolution of the VEGF-inhibitor concentration in plasma, A_1, is described by the following two-compartment pharmacokinetic model [21]:

$$\frac{dA_1(t)}{dt} = -\frac{q}{v_1}A_1(t) - \frac{cl}{v_1}A_1(t) + \frac{q}{v_2}A_2(t)$$
$$\frac{dA_2(t)}{dt} = -\frac{q}{v_2}A_2(t) + \frac{q}{v_1}A_1(t), \tag{S10}$$

where A_1 and A_2 are the concentrations of the VEGF-inhibitor in plasma and peripheral compartments, whose volumes are v_1 and v_2, respectively. Parameters q and cl are the

inter-compartmental and plasma elimination clearance, respectively. We model each VEGF-inhibitor administration of dose D_i at time t_i, $i = 1, ..., \#$ doses, by adding an instantaneous bolus of $\frac{D_i}{v_1}$ to the plasma concentration at the corresponding time point.

Following reference [34], we model the plasma concentration of each drug $j = 1, 2, 3$, G_1^j, by a specific pharmacokinetic model for that drug. We use a mono-compartmental model with non-linear elimination for drug j=1 (Fluororacil):

$$\frac{dG_1^1(t)}{dt} = \frac{-v_{max}}{K_m + G_1^1(t)} G_1^1(t), \tag{S11}$$

where v_{max} and K_m are the maximal degradation rate and the concentration at which degradation is half maximal. We use a three compartment model for drug j=2 (Epirubicin):

$$\frac{dG_1^2(t)}{dt} = -\frac{q_2}{w_1} G_2^2(t) - \frac{q_3}{w_1} G_3^2(t) - \frac{cl_2}{w_1} G_1^2(t) + \frac{q_3}{w_3} G_3^2(t) + \frac{q_2}{w_2} G_2^2(t)$$

$$\frac{dG_2^2(t)}{dt} = -\frac{q_2}{w_2} G_2^2(t) + \frac{q_2}{w_1} G_1^2(t)$$

$$\frac{dG_3^2(t)}{dt} = -\frac{q_3}{w_3} G_3^2(t) + \frac{q_3}{w_1} G_1^2(t) \tag{S12}$$

$$\tag{S13}$$

where G_1^2, G_2^2 and G_3^2 are the drug concentrations in plasma and the two other compartments with corresponding volumes, v_1, v_2 and v_3. Parameters q_2, q_3 and cl_2 are the inter-compartmental and elimination clearances, respectively. We use a mono-compartmental model with linear elimination for 4-hydroxycyclophosphamide, the major active microsomal metabolite of drug j=3 (Cyclophosphamide):

$$\frac{dG^3(t)}{dt} = -\frac{cl_3}{u} G^3(t), \tag{S14}$$

where cl_3 and u are elimination clearance and compartment volume, respectively.

S3 Model initialization and parameterization

S3.1 A quantitative portrait of the individual tumor

Here we explain which data are used and how, to describe relevant quantitative aspects of the individual tumor. Available clinical data at week 0 included histopathological slides and molecular data from core-needle biopsies, as well as MRI of the whole breast. We used these data to initialize and parameterize the mathematical model for each patient. Specifically, cancer and stroma cells were identified and located in representative portions of the histopathological slides and used to determine the initial position of cells and their initial number, see section S3.2 and fig. S12 below. As functional blood vessels were not identifiable in the histopathological slides, we initialized them using DCE-MRI data as explained in section S3.3 below. In this way we were able to mimic observed molecular transport and perfusion in the tumor tissue without having precise initial location of vessels in the simulated

17

portion of tissue. DCE-MRI and molecular data at week 0 were also used to estimate model parameters specific to the patient tumor. In particular, vessel permeability was estimated in each tumor voxel as explained in section S3.5.1 below. Typical permeability values over all voxels of each individual patient were then used in the simulations. The VEGF-*TP53* signaling model was calibrated to agree with the observed gene expression data and TP53 mutation status, see section S3.5.1 below for details. As explained in the same section, we also estimated an average proliferative capacity of tumor cells in each tumor using the PAM50 classification [31, 35], together with measured volumes of xenografts of the same type. PDS of HIF1A pathway was used to validate qualitatively the simulated hypoxic status of each patient at week 0. Each individual tumor was portrayed as described above and listed in table S1 and table S2 below. However, several other parameters, needed to quantify the model dynamics were not directly estimable from the current data at week zero. Therefore, we obtained them from publicly available data whenever possible. Those parameters include biophysical parameters (for example diffusion coefficients and reaction rates), data obtained from other breast cancer patients different than those of the NeoAva study (i.e., drug pharmacokinetics) and volume growth of breast cancer xenografts in mice. For a complete explanation of model parameterization using patients and public data, see section S3.5 below. Finally there were some parameters which were difficult to estimate, because clinical data related to them were not available, nor did we find relevant quantities in the literature. One example of such parameter is the chemosensitivity level. Those response rates, however, were measured in cell cultures after six days [15], and could not be directly applied to our model where the probability of cell killing affects only cells that have passed the G1/S checkpoint at 30 minutes intervals.

To circumvent this problem, we modeled the dose response curve by a cumulative beta distribution $Beta(\alpha, \beta)$ (with α fixed to be 1) that resembles the curve obtained experimentally in reference [15]. We then assumed that 30 minute response rates for each patient can be achieved for a certain unknown value of the parameter β. In addition to β, three other parameters, namely $p_{\text{death}}, p_{\text{birth}}$ and High_V related to vessel creation and deletion, were also calibrated. See section S3.5.3 for detailed description.

S3.2   Cell initialization

To initialize the number and positions of cells, we map cancer and stroma cells identified in the histopathological sections to a 2D computational lattice, where the model is simulated. Given the physical size of a pixel in the histological images ($0.148 \, \mu\text{m}$), we calculate the physical size of a captured imaged to be approximately $230 \, \mu\text{m} \times 310 \, \mu\text{m}$. The number of grid points in each direction of the computational grid is determined by dividing the length of each side by typical size of a cancer cell. Cancer cells vary in sizes, ranging from $10 \, \mu\text{m}$ to $20 \, \mu\text{m}$ in diameter. We chose $10 \, \mu\text{m}$ to ensure similar cell density between captured and projected image. Having determined the size of the grid, the coordinate of each cell identified by pathologists is then divided by the pixel size and rounded to its nearest integer. After rounding, should multiple cells occupy the same coordinates in the simulation grid, they are put in the nearest neighborhood to the grid point so that the cell number matches with the one found in the biopsy slide. Figure S12 shows how the obtained cell positions resemble cell configurations in a histopathological section. This procedure was done for each patient in two different biopsy images that we call Biopsy A and Biopsy B. The results are also shown

18

in fig. S12 together with vessel initialization that is explained below.

S3.3 Vessel initialization

The exact position and permeability of each functional blood vessel in the tumor tissue is unknown. However, as DCE-MRI data describe the perfusion of a contrast agent (CA) in each tumor voxel, they can be used to find vessel configurations and permeabilities that reproduce the observed tumor perfusion. For that, we use a reaction-diffusion equation to model the spatio-temporal distribution of CA, $\mathbf{C}_e(\boldsymbol{x}, t)$, in the extracellular space:

$$\frac{d\mathbf{C}_e(\boldsymbol{x}, t)}{dt} = D_c \nabla^2 \mathbf{C}_e(\boldsymbol{x}, t) + PS(\mathbf{C}_p(t) - \mathbf{C}_e(\boldsymbol{x}, t)) \cdot \mathcal{G}(\boldsymbol{x}, t) \tag{S15}$$

where D_c is the diffusion coefficient of the CA, PS is the permeability surface product of the CA in the vessels and the function $\mathbf{C}_p(t)$ describes the time evolution of the CA concentration inside the vessels. While parameter D_c is known and the function $\mathbf{C}_p(t)$ (also called arterial input function) can be measured in each patient, PS and the vessels location at the start of the therapy, $\mathcal{G}(\boldsymbol{x}, 0)$, are unknown. Thus, our goal is to find vessel configurations and permeabilities that reproduce the observed perfusion in the tumor area. To do that, we make a number of assumptions. Firstly, we use k_{trans}, which we estimated in each tumor voxel using an extended Tofts model (see Materials and Methods), as an approximation of PS [19]. Secondly, we assume all capillaries to be $10\,\mu\text{m}$ in diameter and perpendicular to the simulated cross-section, as in our multi-scale model of therapy response (section S2). An estimate of the number of vessels can thus be computed as $n_v = v_p/v_0$, the ratio of volume occupied by plasma v_p (also measured in each tumor voxel), and that occupied by one vessel v_1. Finally we characterize the spatial distribution of vessels by the minimum distance between any neighboring vessels, d_{sep}. The procedure for vessel initialization in each personalized therapy simulation is then as follows. First, from the histograms of all k_{trans} and v_p related to each voxel, we choose one value. We compute the number of vessels as explained above and assume all have the same permeability PS. We use k_{trans} as an approximation to PS, scaled by $20\pi\,\mu\text{m}$, to account for capillary surface which is a discrete point in our computational grid. Then we test different distributions of n_v vessels in the computational grid using different values of d_{sep}. Numerical simulations of eq. (S15) using those different vessel distributions, produce different CA spatio-temporal distribution, $\mathbf{C}_e(\boldsymbol{x}, t)$. Taking the average in space for each time point we obtain $\mathbf{C}_e(t)$. The total tissue concentration is estimated as:

$$\mathbf{C}(t) = \mathbf{C}_e(t) + v_p \mathbf{C}_p \tag{S16}$$

We select the vessel distribution such that the average of all experimental concentration curves $\mathbf{C}(t)$ in all the voxels with the same value for v_p and k_{trans} is most similar to the patient data. See vessel initialization for the four patients in fig. S12.

S3.4 Initialization of continuous variables

Given initial distribution of cells and vessels as explained above, the oxygen eq. (S5) was ran until steady state give initial concentration of 0 mmHg. The steady state solution of oxygen
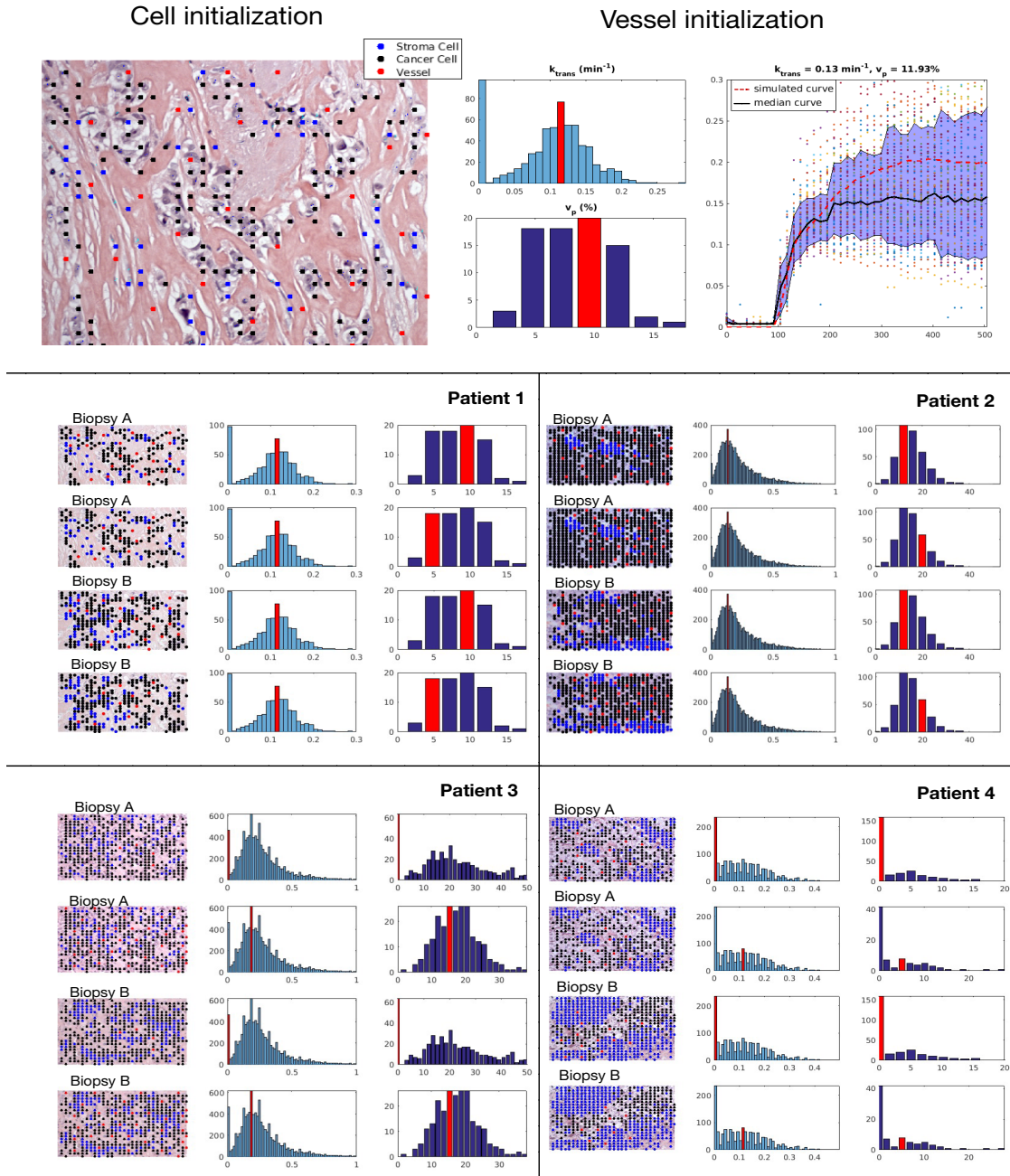
Figure S12: Cell and vessel initialization. The top panel shows an example of cell and vessel initialization from a histopathological slide and histograms of k_{trans} and v_p values obtained from the MR images of the corresponding tumor. Black and blue dots represent cancer and stroma cells, respectively. Those were mapped as described in the text. Red dots represent a selected vessel configuration that mimics the observed perfusion data in that tumor for the choice of k_{trans} and v_p indicated in red in the nearby histograms. The top right image shows the average of all CA concentration curves observed in all tumor voxels with the corresponding value of k_{trans} and v_p. The shaded region indicates 95% intervals of those curves and the red dotted line is the simulated CA concentration for the selected vessel configuration (as described in section S3.3) using the same values of k_{trans} and v_p. The rest of the figure shows 4 panels, each showing cell and vessel initializations for the 4 different patients considered in this study.

is then used as the initial state in the therapy simulation. The rest of spatial continuous variables (VEGF, all drugs and the VEGF-VEGF inhibitor complex) are initialized with zero concentration over the whole domain D. Given the initial oxygen concentration, intracellular levels of VEGF and TP53 of a cell at position $\boldsymbol{x}$ (if any), were initialized by running solvers of (eqs. (S3) and (S4)) until steady state and use those values to initialize $[\text{sVEGF}]_{\boldsymbol{x}}$ and $[\text{TP53}]_{\boldsymbol{x}}$ in each cell. Initial cell cycles are set to be uniformly distributed between 0 and 1. Plasma concentration of each drug is initialized as d/V where d is the adjusted dose assuming height of 160cm and weight of 58.1kg, and V is the estimated plasma compartment volume. (See table S2)

S3.5   Model parameterization and calibration

In this section we discuss the set of parameter values used in the simulations. Several parameters were directly obtained from personal patient's data (see table S2 and section S3.5.1). Other model parameters were taken from published data wherever possible or estimated to approximate physiologic conditions based on appropriate physical arguments (see table S3 and section S3.5.2). Finally, there were a few parameters which were difficult to estimate, either because they are model-specific and clinical data related to them were not available, or because we did not find relevant quantities in the literature. For those parameters, a wide range of values was considered to explore their effects on the resulting treatment outcome and find values that are compatible with the observed treatment outcome of each patient (see table S4 and section S3.5.3).

S3.5.1   Parameters estimated from patient's data

Model simulations were personalized by estimating a number model parameters from the clinical data of each patient. The estimated values for each patient are shown in Table 1. Below, we discuss how those values were derived:

Table S2: Parameter values estimated from patient's data

Parameter	Description (units)	Patient 1		Patient 2		Patient 3		Patient 4	
		Bio A	Bio B	Bio A	Bio B	Bio A	Bio B	Bio A	Bio B
n_c	Initial cancer cells (number)	146	218	386	516	315	333	188	273
n_s	Initial stroma cells (number)	45	72	140	53	149	101	339	148
$T_{\min}$	Minimum cell cycle duration (days)	14.69		3.74		3.74		3.74	
k_7	Basal p53 synthesis rate (min^{-1})	0.002		0.012		0.0004		0.002	
k_8''	Maximal p53 effect in VEGF production (min^{-1})	-0.002		-0.0037		-0.0002		0.002	
		Cond A	Cond B	Cond A	Cond B	Cond A	Cond B	Cond A	Cond B
n_v	Initial blood vessels (number)	27	45	27	45	4	35	14	9
r_{Gi}	Chemotherapies permeability (min^{-1})	8.17	8.17	8.80	8.80	0.42	13.5	0.42	6.96
r_A	Avastin permeability (min^{-1})	0.08	0.08	0.08	0.08	0.0042	0.135	0.0042	0.07
d_{G1}	Fluorouracil dose (mg m^{-2})	600		600		600		600	
d_{G1}	Epirubicin dose (mg m^{-2})	100		100		100		100	
d_{G3}	Cyclophosphamide dose (mg m^{-2})	600		600		600		600	
d_A	Bevacizumab dose (mg kg^{-1})	15		15		0		0	

- n_c and n_s: Cancer and stroma cells were manually identified by an experienced pathologist in the available histological sections at week 0, as described in the Histopathology section of Materials and Methods. To capture some of the heterogeneity observed in the

histological slides, the pathologist identified cells in two different biopsy areas (Bio A and Bio B) with different cell densities and distributions. Table S2 displays the total number of cancer and stroma cells counted in each area.

- T_{min}: The minimum cell cycle duration of cancer cells was roughly approximated as the doubling time of cancer cells, estimated in each patient from gene expression data of his tumor (PAM50 classification and proliferation score) and volume growth data from untreated mice xenografts. Specifically, for tumors with Luminal or Basal PAM50 classification, we used average volume data from 11 Luminal- and 5 Basal-like mice xenografts, respectively. Given the average volumes s_0 and s_1 in two time points t_0 and t_1, respectively, we use the following formula to compute cell doubling times $T_{min} = ((t1 - t0) * \log(2))/(\log(s_1/s_c) - \log(s_0/s_c))$, where s_c is the volume of a cancer cell. We used $s_c = 4.189 \times 10^{-6} mm^3$ assuming spherical cells or radius 10 microns. From reference [18], we estimated $s_0 = 128.6364$ at $t = 0$ days and $s_1 = 187.6364$ at $t_1 = 8$ days for Luminal xenografts and $s_0 = 65.2000$ at $t = 0$ days and $s_1 = 198.2000$ at $t_1 = 6$ days for Basal xenografts. As patient 3 was classified as HER2 and no HER2-like xenograft was available, we looked at the proliferation score of that patient (patient 3 score was 2.134). We found that it was very similar to the proliferation scores of basal patients (patient 2 score was 2.3730 and patient 4 score was 2.035). Thus, we decided to use the same value of T_{min} for those Basal and HER2 tumors.

- k_7 and k_8'': We used VEGF and TP53 expression data to calibrate our VEGF-TP53 signaling model. As shown in section S1, the four patients analyzed have very different levels of VEGF and TP53 expression. For instance, patient 1 has approximately average expression of VEGF and TP53 while patient 3 has very high expression of VEGF and very low of TP53. We found that the expression patterns of all four patients can be mimicked by modulating only k_7 and k_8'' out of the 8 parameters in the VEGF-TP53 signaling model (eqs. (S3) and (S4)). The other 6 parameters were taken from the literature as explained in next section.

- n_v: The initial number of vessels was estimated as $n_v = v_p/v_0$ where v_p represents is the tissue percentage occupied by blood. These was obtained from DCE-MRI in each tumor voxel. We call v_0 the volume occupied by one vessel, that we assume is 10 microns in diameter and perpendicular to the simulated cross-section. Simulations in fig. 2 use the mode of v_p observed by MRI in each patient. However, there are tumor portions where these values can be considerably different. To address the heterogeneity in perfusion, we explored other plausible combinations, keeping k_{trans} at a typical value and varying v_p values (high $v_p = 20.12$, typical $v_p = 10.4$, low $v_p = 6.3$). Different v_p give rise to different number of vessels, so that more drug and oxygen can be distributed very differently in the tissue and thus potentially impact the outcome. Low v_p values indicate limited delivery of oxygen and thus reduced tumor growth. Varying the v_p values did not change the outcome across different configurations. (fig. S17)

- r_{G^i}: Chemotherapies permeabilities. As the molecular weight of the three different chemotherapies is comparable with that of CA Gandolinium, we use k_{trans} as an approximation of PS. Liu et al. [19] observed that the mean k_{trans} value was 18% lower than the PS value, with a maximum underestimation of 25% when k_{trans} is greater

than 0.05 min^{-1}. We have therefore investigated the impact of underestimation of permeability in fig. S18.

- r_A: Avastin permeability. As the molecular weight of avastin is two orders of magnitude higher than Gadolinium [11, 12]. Permeability of Avastin is scaled by 0.01 to accommodate its larger molecular weight.

- d_{G^1}, d_{G^2}, d_{G^3} and d_A: The adjusted drug dosages for each chemotherapeutic drug is calculated by the product of unit dose and patient's body surface area (BSA). BSA is calculated using Du Bois formula BSA $= 0.007184 \times W^{0.425} \times H^{0.725}$, where W and H are 58.1 kg and 160 cm respectively. Adjusted dosage for avastin is calculated by multiplying unit dose by patient's weight, W, where $W = 58.1$ kg. Same weight and height are used for calculation of adjusted dose of all patients as individual data were not accessible at the time of our study.

S3.5.2 Model parameters obtained from public data

Parameters derived from the literature are shown in table S3. When needed, additional explanations are provided below.

Table S3: Parameter values obtained from public data

Parameter	Description	Value	Units	Source
k_ϕ	Oxygen concentration at half-maximal cycle speed	1.4	mmHg	[28]
k_7'	Degration rate of p53 by oxygen	0.01	min^{-1}	[28]
K_{TP53}	Oxygen concentration for half-maximal TP53 degredation	0.01	mmHg	[28]
k_8	Synthesis rate of VEGF	0.002	min^{-1}	[28]
k_8'	Reaction rate of p53 with VEGF	0.01	min^{-1}	[28]
J_5	sVEGF concentration for half-maximal sVEGF production	0.04	μg mL^{-1}	[28]
K_{VEGF}	Oxygen concentration for half-maximal VEGF degradation	0.01	mmHg	[28]
D_k	Oxygen diffusion coefficient	1.05 x 10^5	μm^2 min^{-1}	[7]
r_k	Oxygen supply rate	1.88 x 10^4	min^{-1}	[28]
K_0	Oxygen concentration in the blood	20	mmHg	[28]
ϕ_k	Oxygen consumption rate	900	min^{-1}	[13, 37]
K_1	Oxygen concentration for half-maximal consumption	2.5	mmHg	[13]
D_v	VEGF diffusion coefficient	3.52 x 10^3	μm^2 min^{-1}	[14]
a	VEGF secretion slope	6.66×10^{-6}	min^{-1}	[4, 28]
b	VEGF secretion intercept	-1.10×10^{-6}	μg mL^{-1}min^{-1}	[4, 28]
k_a	VEGF association rate to Avastin	7.4×10^{-1}	μg^{-1} mL min^{-1}	[30]
k_d	VEGF dissotiation rate from Avastin	1.76×10^{-3}	min^{-1}	[30]
ψ_v	VEGF decay rate	1.0 x 10^{-2}	min^{-1}	[28]
D_A	Avastin diffusion coefficient	2.4 x 10^3	μm^2 min^{-1}	[16]
ψ_C	Complex decay rate	1.0 x 10^{-2}	min^{-1}	[28]
D_{G^i}	Chemotherapies diffusion coefficient	9.6 x 10^3	μm^2 min^{-1}	[6]
ψ_{G^j}	Chemotherapies decay rate	1.0 x 10^{-2}	min^{-1}	[24]
v_1	Avastin plasma compartment volume	2.66×10^3	mL	[21]
v_2	Avastin peripheral compartment volume	2.76×10^3	mL	[21]
q	Avastin intercompartmental clearance	0.412	mL min^{-1}	[21]
cl	Avastin elimination clearance	0.144	mL min^{-1}	[21]
v_{max}	Fluororacil maximal degradation rate	1.75	μg mL^{-1} min^{-1}	[34]
k_m	Fluororacil half-maximal concentration	27	μg mL^{-1}	[34]
w_1	Epirubicin plasma compartment volume	18×10^3	mL	[34]
w_2	Epirubicin peripheral compartment volume	957×10^3	mL	[34]
w_3	Epirubicin peripheral compartment volume	25×10^3	mL	[34]
q_2	Epirubicin intercompartmental clearance	0.918×10^3	mL min^{-1}	[34]
q_3	Epirubicin intercompartmental clearance	0.25×10^3	mL min^{-1}	[34]
cl_2	Epirubicin elimination clearance	0.983×10^3	mL min^{-1}	[34]
u	Cyclophosphamide plasma compartment volume	2430×10^3	mL	[34]
cl_3	Cyclophosphamide elimination clearance	3.93×10^3	mL min^{-1}	[34]
Δx	Space interval	10	μm	[17, 20]
Δt	Time interval of cell cycle update	30	min	[28]
Δv	Vessel update interval	720	min	[23]
Low$_V$	Lower VEGF angiogenic threshold	10^{-6}	μg mL^{-1}	[25]
α	FEC dose-response shape	1	dimensionless	[15]

- r_k: Oxygen supply rate is calculated as the product of vessel permeability to Oxygen and vessel surface-to-volume ratio. Vessel permeability to Oxygen is 6 cm/min, calculated by [28]. In our case, the surface-to-volume ratio is $2\pi RL/\Delta x^3$, where R and L are the vessel radius and length, $\Delta x/2$ and Δx respectively.

- a and b: In each cell, we model the production rate of extracellular VEGF as a function of the VEGF expression. We found from reference [22] that, in breast tumor tissue, VEGF concentration ranges from approximately 20 to 70 pg mL^{-1}. We choose a linear function such that: when oxygen is at 20 mmHg, average extracellular VEGF concentration is at 20 pg mL^{-1} while when oxygen is at 3.8 mmHg, VEGF concentration is at

$70 \, \mathrm{pg} \, \mathrm{mL}^{-1}$. By solving the equation at equilibrium, i.e. the derivative at 0, and substituting the decay rate as $0.01 \, / \, \mathrm{min}$ [28], we can calculate the corresponding production rate, and hence define the linear relationship between production rate and VEGF expression. At steady state, the corresponding VEGF expression levels are 0.19487 and 0.26993 respectively. Therefore the linear relationship between $VEGF_s$ and r_v is defined as: $r_v = a * [VEGF_s] + b$, where $a = 6.661338 \times 10^{-6}$, $b = -1.098095 \times 10^{-6}$.

- Δx: The value was chosen allowing modeling mean size of tumor capillaries (10 microns in diameter [17]) and cells ($10 - 20$ microns in diameter [20]) using the same computational grid. The resulting physical size of the simulation grid is also coherent with the size of captured digital image.

- Δv: Time of vessel update. As the formation and retraction of vessels happens in the order or hours to days [23], we set this parameter to be 12 hours. Given this value we then scale the probabilities of birth p_{birth} and death p_{death}.

- α: Shape of dose-response curve. For $\alpha = 1$, the shape of the beta distribution $Beta(\alpha, \beta)$ approximates FEC dose-response data obtained in *in vitro* cultures of breast cancer cells derived from 140 chemotherapy-naïve patients at the time of primary surgery [15].

S3.5.3   Calibrated parameters

Four model parameters were calibrated as it was not possible to estimate them directly from clinical data nor we did find relevant quantities in the literature. Moreover, in the present study we were not able to estimate them using longitudinal MRI data. A major difficulty for that was that reliable tumor volume comparison between time points relies on accurate co-registration of the scanning. Since breast are compressible and the size is dependent on the time point during menstruation, it is currently very hard for our experts in medical physics to align the breast and calculate the change in volume. This is in principle not impossible, by means of accurate statistical modeling that compensates for modifying factors. But currently this is beyond the scope of this paper. In the present paper, we run simulations using a wide range of values of those four parameters and their effects on the resulting treatment outcome was observed. We then select values that are compatible with the observed treatment outcome of each patient. This was possible because we have selected patients with either a complete or no response by MRI at 12 weeks of treatment, as explained in section Patients and treatment of the manuscript. Table S4 indicates the selected values used in the simulations of each patient and the figures showing the sweeps of that parameter exploring the effects on treatment outcomes. More details about each of the four parameters are given below.

A parameter we found having a large impact on the treatment outcome is the chemosensitivity level, β of each individual patients. As the chemosensitivity level become higher, cancer cells are more susceptible to chemotherapeutic drugs after each injection. In fig. S13, we demonstrate the impact of 7 different levels, low $\beta = 2000, 4000$, medium $\beta = 6000, 8000$, and high $\beta = 10000, 12000$. As a result, reduction of number of cancer cells increases in all patients as β increases, indicated by boxplots in fig. S13, with the exception of cases of
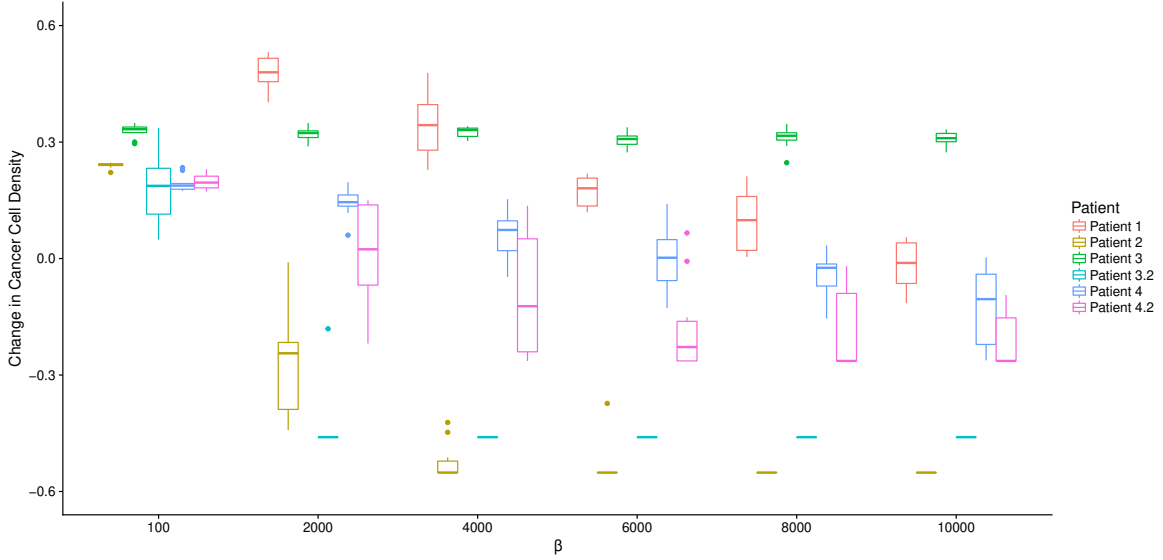
25

Figure S13: Comparison of simulated cancer cell densities for different chemosensitivity level β. Each of the box plots represents difference in cancer cell densities comparing week 12 to the beginning of treatment in 10 simulations. Used chemosensitivity levels were β, low $\beta = 100, 2000, 4000$, medium $\beta = 6000, 8000$, and high $\beta = 10000, 12000$

patient 3 and 4 in which perfusion was poor. Out of all six levels, we are able to reproduce the treatment outcome for all patients when $\beta = 6000$. This demonstrates the importance of highly accurate estimates of this parameter.

Functional blood vessels can be created when the extracellular VEGF level is within an appropriate interval, with upper level denoted by High_V. We therefore tested its effect on treatment outcome. Figure S14 shows studies of five biologically feasible values of $\text{VEGF}_{\text{high}} = 1 \times 10^{-5} \, \text{mg mL}^{-1}$, $5 \times 10^{-5} \, \text{mg mL}^{-1}$, $1 \times 10^{-4} \, \text{mg mL}^{-1}$, $5 \times 10^{-4} \, \text{mg mL}^{-1}$ and $1 \times 10^{-3} \, \text{mg mL}^{-1}$, while keeping other parameters fixed. Higher thresholds allow more and more vessels being created during the course of the treatment. For patient 1 and 2, since Bevacizumab was administered during the course of treatment, extracellular VEGF concentration was always kept below the lower threshold. We observed no difference in treatment outcome at all VEGF thresholds. For patient 3 and 4, even though VEGF was not inhibited by Bevacizumab, newly-created vessels in poorly-perfused tissues were not able to efficiently deliver drugs to the tissue. Thus no significant differences were observed in simulations under different threshold levels. In well-perfused cases, we were able to reproduce outcomes for patient 4 when VEGF threshold was set to be higher than $1 \times 10^{-3} \, \mu\text{g/mL}$. At $1 \times 10^{-4} \, \mu\text{g/mL}$, we were able to reproduce patient 1, 2 and 3. These values are well above reported physiological VEGF concentrations in the order of pg mL^{-1}. We also compare values obtained by calibration with reported VEGF thresholds between normal and aberrant angiogeneis in [29]. For that we transform the experimentally obtained rate units to our concentrations using the data reported in that paper of 4 hours experiments and $5\text{x}10^4$ cells. Namely, dividing by 6 hours and scaling the number of cells we obtain a VEGF threshold between $4 \times 10^{-4} \, \mu\text{g/mL}$
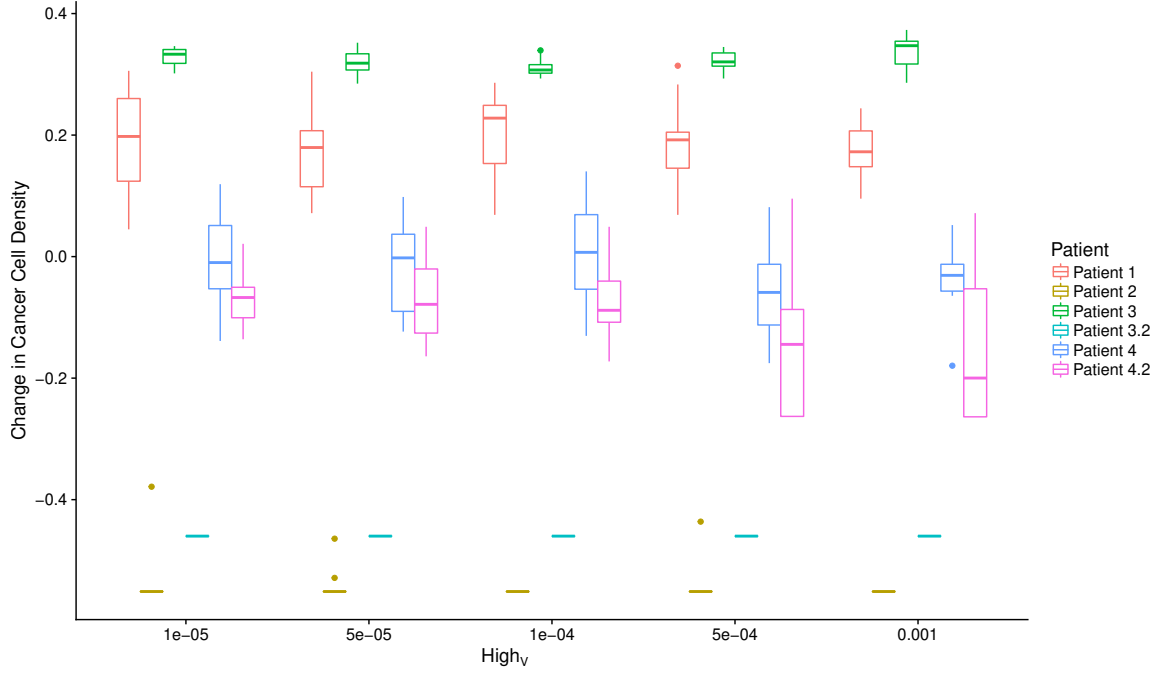
26

Figure S14: Comparison of simulated cancer cell densities for different VEGF thresholds. Each of the box plots represents difference in cancer cell densities comparing week 12 to the beginning of treatment in 10 simulations. Used upper VEGF threshold for angiogenesis were $\text{High}_V = 1 \times 10^{-5}\,\text{mg}\,\text{mL}^{-1}$, $5 \times 10^{-5}\,\text{mg}\,\text{mL}^{-1}$, $1 \times 10^{-4}\,\text{mg}\,\text{mL}^{-1}$, $5 \times 10^{-4}\,\text{mg}\,\text{mL}^{-1}$ and $1 \times 10^{-3}\,\text{mg}\,\text{mL}^{-1}$

and $8 \times 10^{-4}\,\mu\text{g/mL}$, which nicely approximate the values we obtained by calibration.

We then investigated how the number of newly-created vessel affect the treatment outcome given the upper level VEGF threshold is high enough to allow vessel creation. Figure S15 shows studies of six different values of $p_{\text{birth}} = 0.0005, 0.002, 0.01, 0.05, 0.1,$ and 0.5. Higher probabilities allow more vessels being created during the course of the treatment. For patient 1 and 2, since Bevacizumab was administered during the course of treatment, extracellular VEGF concentration was always kept below the lower threshold. Regardless of the probability of vessel birth, no vessel would be created as a result. Thus we observed no difference in treatment outcome at all values. For patient 3 and 4, even though VEGF was not inhibited by Bevacizumab, newly-created vessels in poorly-perfused tissues were not able to efficiently deliver drugs to the tissue.(See fig. S15b) Thus no significant differences were observed in simulations under different threshold levels. In well-perfused cases, we were able to reproduce outcomes for patient 4 when probability is set higher than 0.01. At $p_{\text{birth}} = 0.0002$, we were able to reproduce patient 1, 2 and 3.

Finally we also looked at how the number of vessel being deleted affect the treatment outcome. Figure S16 shows studies of five different values of $p_{\text{death}} = 0.0001, 0.001, 0.01,$ and 0.5.

Higher p_{death} allows more vessels to be deleted. For patient 1 and 2, VEGF concentration was kept below the lower threshold as a result of Bevacizumab. For $p_{\text{death}} < 0.1$, we observed no significant difference in treatment outcome, while with $p_{\text{death}} \geq 0.1$, no vessels were left before the end of treatment. Neither oxygen nor drugs could be delivered to the tissue, no cells could proliferate or killed. For patient 3 and 4, the deletion of poorly-perfused vessels did not affect the outcome of treatment; While in well-perfused tissues, without the inhibition of bevacizumab, the birth and the death of vessels counteracted with each other, resulting in no difference in cancer cell density at the end of week 12 across different p_{death}.

Table S4: Calibrated parameter values

Parameter	Description (Units)	Value				Parameter sweeps
β	FEC dose-response sensitivity (non dimensional)	6000 - 10000 (6000)				fig. S13
p_{death}	vessel death probability	0.0001 - 0.01 (0.0001)				fig. S16
		Patient 1	Patient 2	Patient 3	Patient 4	
High_V	upper VEGF angiogenic threshold (μg mL^{-1})	10^{-4}	10^{-4}	10^{-4}	2×10^{-3}	fig. S14
p_{birth}	vessel birth probability	0.002	0.002	0.002	0.01	fig. S15

S4   Computational details

The code to simulate the mathematical model is written in Python 3.6.2 and available at `bitbucket.org/xlai/codeavastin-py.git`. It is structured in a modular way for easy debugging and reusability and all files are properly documented. All differential equations were solved with finite element software FEniCS [2]. Simulations were run on the Abel Cluster, owned by the University of Oslo and Uninett/Sigma2, and operated by the Department for Research Computing at USIT,the University of Oslo IT-department. http://www.hpc.uio.no/ Below we briefly summarize the main algorithm in algorithm 1 and describe in detail numerical methods used to solve the different differential equations that integrates all the modules of the mathematical model.

S4.1   Numerical solution of ODEs and PDEs

S4.1.1   Solving the oxygen concentration equation

We consider the steady state version of eq. (S5) ($s_K = 0$). The resulting nonlinear partial differential equation was solved numerically using a finite element approximation. The unknown K was approximated using continuous piecewise linear defined relative to a uniform triangulation $\mathcal{T}$ of the lattice L. The resulting nonlinear algebraic equation was solved using Newton's method with tolerance $\epsilon = 10^{-6}$. The equation was then solved using a direct (and thus exact) solver.

S4.1.2   Solving the coupled system of equations of VEGF/VEGF-inhibitor complex

We consider the steady state version of eq. (S6)–eq. (S8) ($s_V, s_A, s_C = 0$). The resulting system of nonlinear, partial differential equations were solved numerically using a finite element
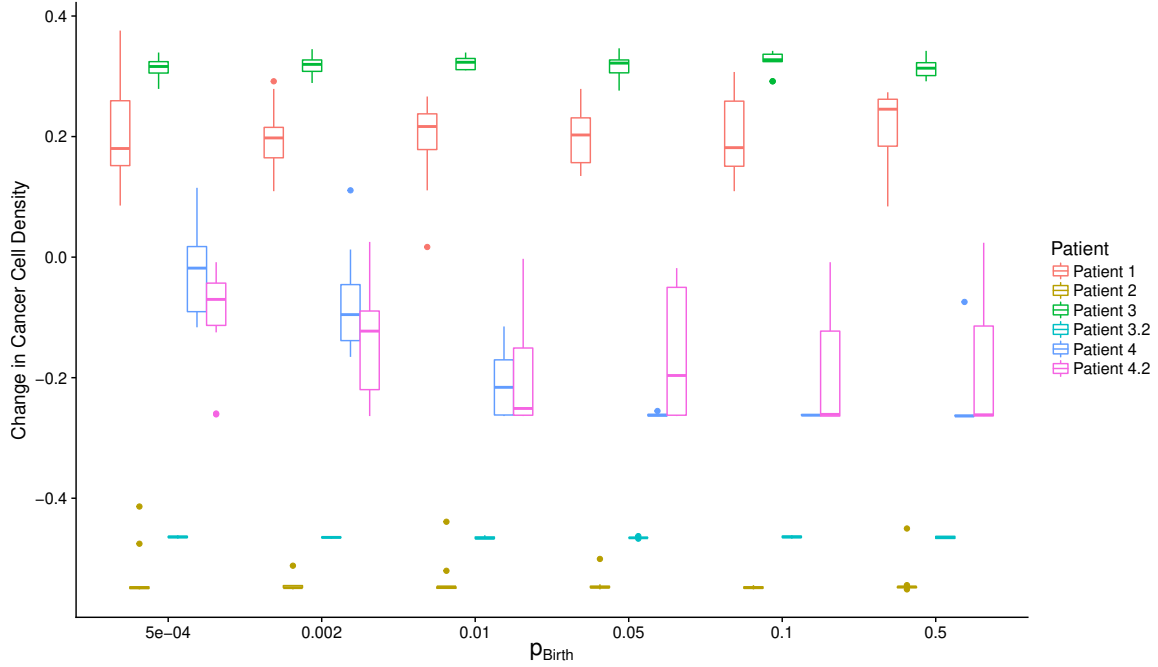
(a) Comparison of simulated cancer cell densities between different probability of vessel birth, p_{birth}.
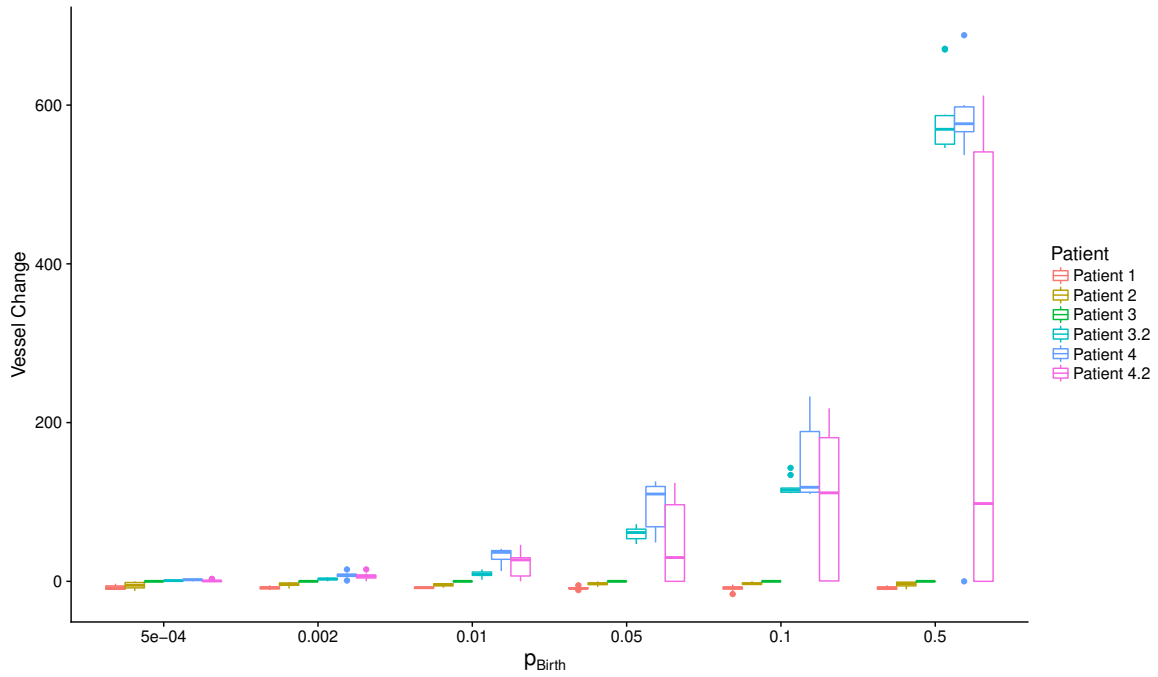
(b) Comparison of vessel changes between different probability of vessel birth, p_{birth}.

Figure S15: Each of the box plots represents difference in cancer cell densities comparing week 12 to the beginning of treatment in 10 simulations. Used vessel birth probabilities were $p_{birth} = 0.0005, 0.002, 0.01, 0.05, 0.1,$ and 0.5
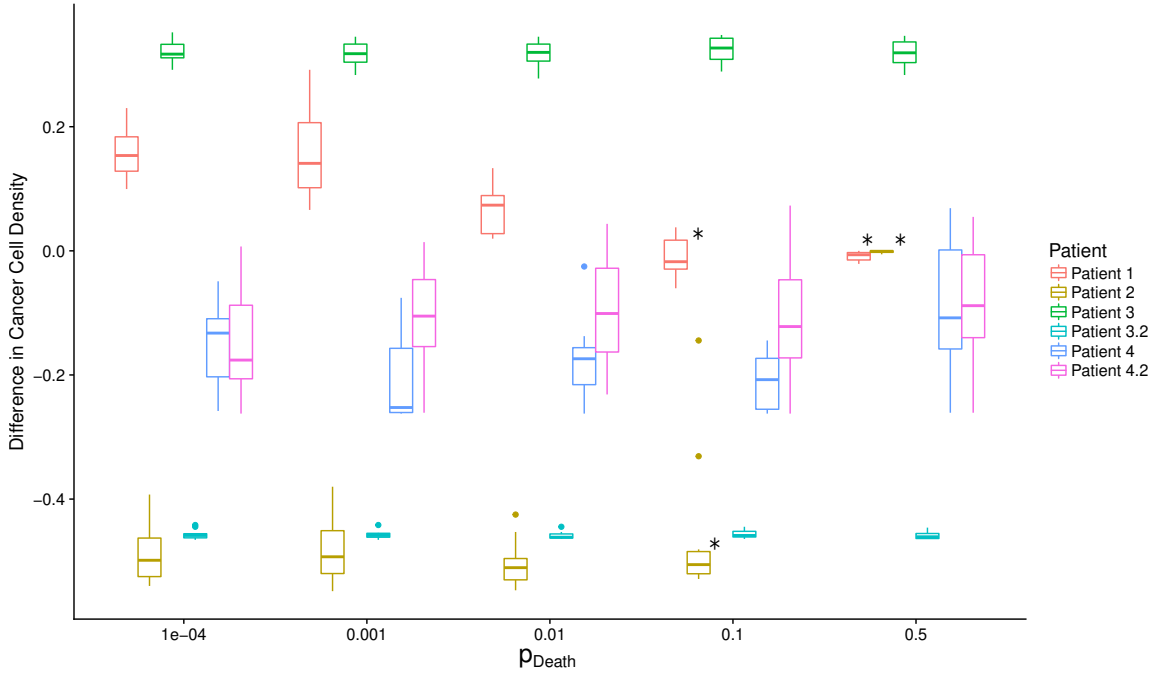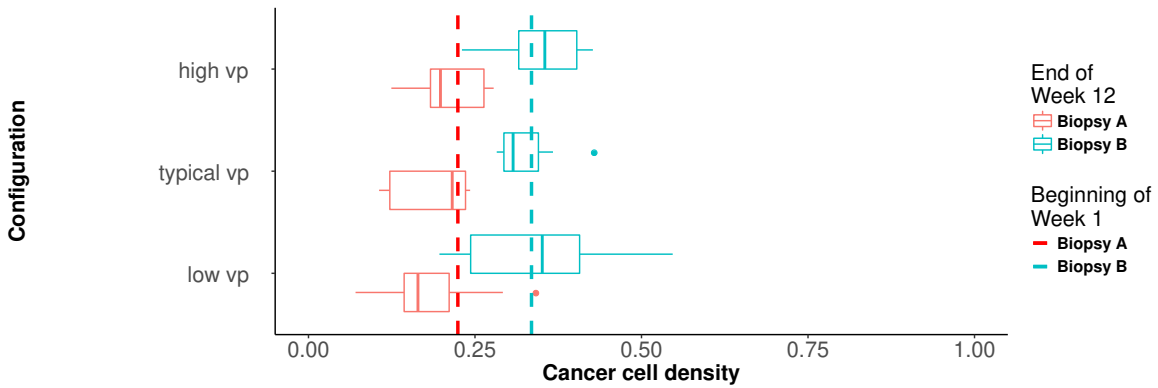
Figure S16: Comparison of simulated cancer cell densities between different probability of vessel death, p_{death}. The x-axis indicates the probability of death of a vessel if VEGF is within the range, * Simulations terminated when no vessels were left. Results shown were the difference between termination and the beginning of each simulation.

(a) Patient 1

Figure S17: Effect of perfusion heterogeneity on treatment outcomes. For patient 1, cell at the end of the treatment period are shown for two observed initial cell configurations (biopsy 1 in red and biopsy 2 in blue). Boxes represent cell densities after 12 weeks in 10 simulations using $k_{\text{trans}} = 0.13$ and one value of $v_p = 6.3, 10.4, 20.12$ for each patient.

Procedure 1 Main algorithm

1: Initialize computational mesh $\mathcal{T}$ corresponding to the regular square lattice L (cf. section S2).

2: Initialize vascular lattice representation $\mathcal{G}(\cdot, 0)$ and cellular lattice representation $\mathcal{L}(\cdot, 0)$ based on histopathological data described in section S1.2.

3: Compute the initial oxygen concentration $K(\cdot, 0)$ by solving eq. (S5) with $s_K = 0$ (cf. section S2.4.1).

4: Define the initial condition for the cell cycle ϕ based on a uniform random distribution:

$$\phi_{\mathbf{x}}(0) \in \mathcal{U}(0,1) \quad \forall \mathbf{x} \in L,$$

and compute the intracellular levels of [TP53] and [sVEGF] at initial time ($t = 0$) by solving eq. (S3) and eq. (S4), respectively, using the initial oxygen concentration $K(\cdot, 0)$.

5: Define initial chemotherapy concentrations by letting $G^j(\cdot, 0) = 0$ for $j = 1, 2, 3$. Define initial conditions for V, A and C by letting $V(\cdot, 0) = 0$, $A(\cdot, 0) = 0$ and $C(\cdot, 0) = 0$.

6: Define initial intravascular chemotherapy concentrations and initial intravascular VEGF-inhibitor concentrations by letting $G_j(0) = 0$ for $j = 1, 2, 3$ and $A_1(0) = 0$. Solve eq. (S10)-eq. (S12) given dose d_i for $G_j, j = 1, 2, 3$ and A_1 at time $t_i, i = 1, \ldots, N$ to get $G_j(t_i)$ for $j = 1, 2, 3$ and $A_1(t_i)$

7: Set $t^1 = \Delta t = 30$ min, $n = 1$

8:

9: **while** $t^n \leq T$ **do**

10:    Compute $K(\cdot, t^n)$ by solving eq. (S5) with $s_K = 0$ (cf. section S2.4.1).

11:    Compute $V(\cdot, t^n)$, $A(\cdot, t^n)$, $C(\cdot, t^n)$ by solving eq. (S6)– eq. (S8) (cf. section S4.1.2).

12:    Compute G^j for $j = 1, 2, 3$ by solving eq. (S9) (cf. section S2.4.5).

13:    Compute [TP53]$(\cdot, t^n)$ and [sVEGF]$(\cdot, t^n)$ by solving eq. (S3) and eq. (S4) and compute $\phi(\cdot, t^n)$ by solving eq. (S2) using $K(\cdot, t^n)$.

14:    Compute $\mathcal{L}(\cdot, t^n)$ based on cellular automaton rules described.

15:    Set $t^n = t^{n-1} + \Delta t$, $n = n + 1$.
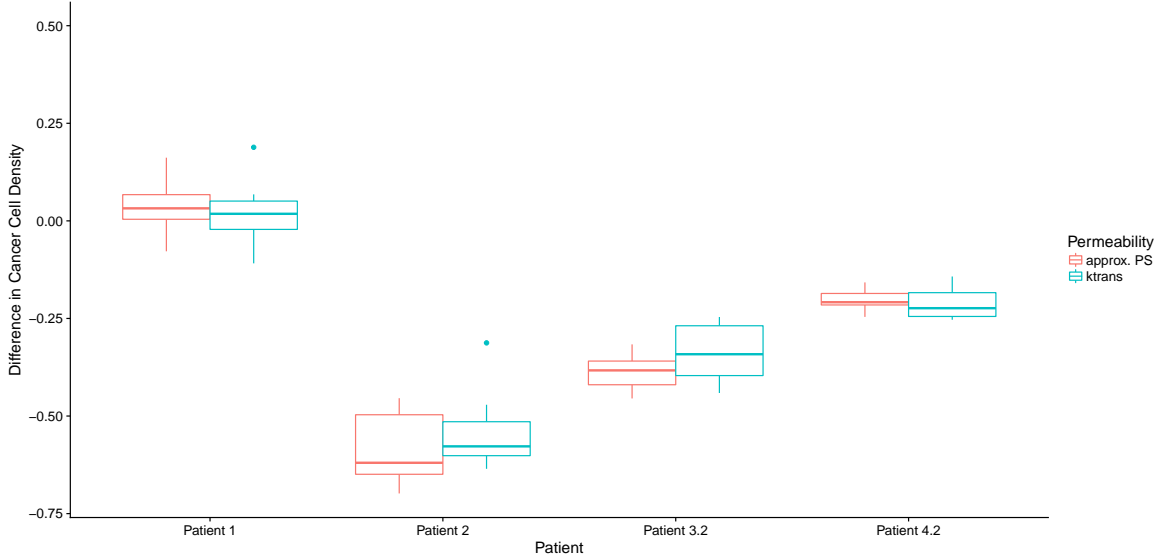
16: **end while**

Figure S18: Comparison of simulated cancer cell densities between estimated k_{trans} values obtained from MRI data and their corresponding values that are 25% higher for all patients.

approximation. The unknowns V, A and C were approximated using continuous piecewise linears defined relative to a uniform triangulation $\mathcal{T}$ of the lattice L. The resulting nonlinear system of algebraic equations were solved using Newton's method with tolerance $\epsilon = 10^{-6}$. The linear systems of equations were solved using a direct (and thus exact) solver.

We also compared these solutions V, A and C, computed using the steady state version of eq. (S6)–eq. (S8) with solutions computed using a forward Euler discretization of the corresponding parabolic equations ($s_V, s_A, s_C = 1$) over the time interval $\Delta t = 30min$. The two sets of solutions agreed well, thus indicating that solving the steady state equations was sufficient.

S4.1.3   Solving the chemotherapy concentration equations

For each $j = 1, 2, 3$, we solved eq. (S9) using a Crank-Nicolson scheme in time and a finite element method in space. Again, we approximated $G^j(\cdot, t^n)$ for each n using continuous piecewise linears defined relative to the same uniform triangulation $\mathcal{T}$ of the lattice L, and solved the resulting linear systems of equations using a direct solver.

S4.1.4   Solving ODE systems of intracellular TP53 and VEGF signaling

We chose 4th-order Runge-Kutta scheme implemented in FEniCS with fixed timestep to solve eq. (S3)-eq. (S4) in section S2.3.2 for each cell for its ease of implementation over the function space.

S4.2   Cellular automaton updates

For each cell at $\boldsymbol{x} = (x_i, x_j) \in \mathcal{L}$ with cell cycle $\phi_{\boldsymbol{x}} \geq 1$, the cell is killed with probability drawn from a random Beta distribution $Beta(1, \beta), \beta > 0$. If the cell is not killed, a new

cell is placed at $\boldsymbol{x}' \in (x_{i\pm1}, x_{j\pm1})$ with the highest K. No cell is placed if no free spaces is available in the neighborhood. $\phi_{\boldsymbol{x}}$ and $\phi_{\boldsymbol{x}'}$ are set to 0. [TP53] and [VEGFs] are set to zero at both $\phi_{\boldsymbol{x}}$ and $\phi_{\boldsymbol{x}'}$. The sequence of updates for proliferation-ready cells is asynchronous such that the new state of a cell affects the calculation of states in neighboring cells.

S5   Other

This section contains other images to supplement the main text of the paper.

(a) **Simulations of alternative therapy of patient 1, in which only Epirubicin and Cyclophosphamide were administered at full dose every 3 weeks**.

(b) **Simulations of alternative therapy of patient 1, in which only Epirubicin and Cyclophosphamide were administered at full dose every 1 week**.
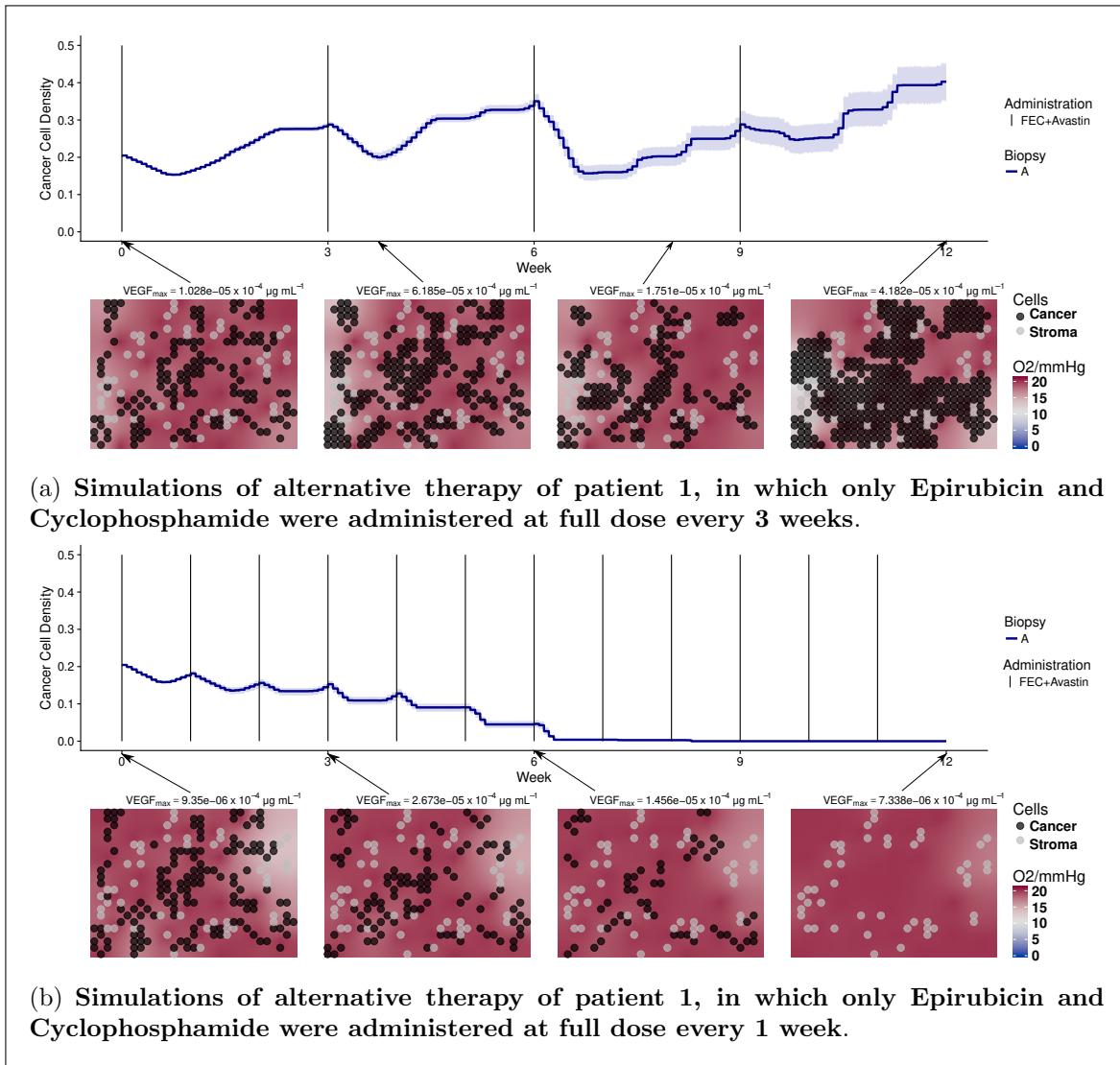
Figure S19: Time evolution of cancer cell density under two different drug schedules with epirubicin and cyclophosphamide for patient 1. Each line represents the average cancer cell density of 10 independent stochastic simulations. The corresponding color band indicates the 95% bootstrap confidence interval. Lower panel of each figure shows the spatial distribution of cancer and stroma cells for a representative simulation of the biopsy portion A for the patient. Background color represents oxygen pressure in mmHg.

References

[1] Alarcón T, Byrne HM, Maini PK. A multiple scale model for tumor growth. Multiscale Model Sim 2010;3(2):440.

[2] Alnæs MS, Blechta J, Hake J, Johansson A, Kehlet B, Logg A, et al. The FEniCS Project Version 1.5. Archive of Numerical Software 2015;3(100).
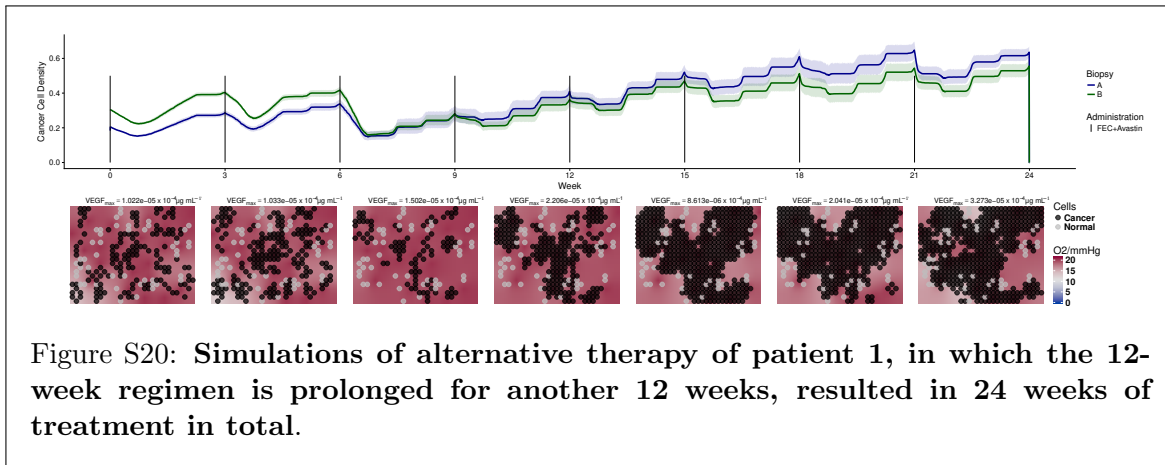
Figure S20: **Simulations of alternative therapy of patient 1, in which the 12-week regimen is prolonged for another 12 weeks, resulted in 24 weeks of treatment in total**.

[3] Conklin J, Heyn C, Roux M, Cerny M, Wintermark M, Federau C. A Simplified Model for Intravoxel Incoherent Motion Perfusion Imaging of the Brain. Am J Nephrol 2016;37(12):2251–2257.

[4] Dabrosin C, Chen J, Wang L, Thompson LU. Flaxseed inhibits metastasis and decreases extracellular vascular endothelial growth factor in human breast cancer xenografts. Cancer Lett 2002;185(1):31–37.

[5] Daşu A, Toma-Daşu I, Karlsson M. Theoretical simulation of tumour oxygenation and results from acute and chronic hypoxia. Phys Med Biol 2003;48(17):2829.

[6] El-Kareh AW, Secomb TW. A mathematical model for comparison of bolus injection, continuous infusion, and liposomal delivery of doxorubicin to tumor cells. Neoplasia 2000;2(4):325–338.

[7] Grote J, Süsskind R, Vaupel P. Oxygen diffusivity in tumor tissue (DS-Carcinosarcoma) under temperature conditions within the range of 20–40 °C. Pflügers Archiv 1977;372(1):37–42.

[8] Grøvik E, Bjørnerud A, Storås TH, Gjesdal KI. Split dynamic MRI: Single bolus high spatial–temporal resolution and multi contrast evaluation of breast lesions. J Magn Reson Imaging 2014;39(3):673–682.

[9] Hales PW, Kirkham FJ, Clark CA. A general model to calculate the spin-lattice (T1) relaxation time of blood,accounting for haematocrit, oxygen saturation and magnetic field strength. J Cerebr Blood F Met 2015;.

[10] Hlushchuk R, Ehrbar M, Reichmuth P, Heinimann N, Styp-Rekowska B, Escher R, et al. Decrease in VEGF expression induces intussusceptive vascular pruning. Arterioscler Thromb Vasc Biol 2011;31(12):2836–2844.

[11] Inc B. Gadovist 1.0: Product Monograph; 2018.

[12] Inc G. Avastin: Highlights of Prescribing Information; 2017.

[13] Kelly C, Brady M. A model to simulate tumour oxygenation and dynamic [18F]-Fmiso PET data. Phys Med Biol 2006;51(22):5859–5873.

[14] Köhn-Luque A, De Back W, Yamaguchi Y, Yoshimura K, Herrero M, Miura T. Dynamics of VEGF matrix-retention in vascular network patterning. Phys Biol 2013;10(6):066007.

[15] Konecny G, Fritz M, Untch M, Lebeau A, Felber M, Lude S, et al. HER-2/neu over-expression and in vitro chemosensitivity to CMF and FEC in primary breast cancer. Breast Cancer Res Treat 2001;69(1):53–63.

[16] Kuznetsov MB, Kolobov AV. Transient alleviation of tumor hypoxia during first days of antiangiogenic therapy as a result of therapy-induced alterations in nutrient supply and tumor metabolism–analysis by mathematical modeling. J Theor Biol 2018;.

[17] Less JR, Skalak TC, Sevick EM, Jain RK. Microvascular architecture in a mammary carcinoma: branching patterns and vessel dimensions. Cancer Res 1991;51(1):265–273.

[18] Lindholm EM, Kristian A, Nalwoga H, Krüger K, Nygård S, Akslen LA, et al. Effect of antiangiogenic therapy on tumor growth, vasculature and kinase activity in basal-and luminal-like breast cancer xenografts. Mol Oncol 2012;6(4):418–427.

[19] Liu HL, Chang TT, Yan FX, Li CH, Lin YS, Wong AM. Assessment of vessel perme-ability by combining dynamic contrast-enhanced and arterial spin labeling MRI. NMR Biomed 2015;28(6):642–649.

[20] Liu Z, Lee Y, hee Jang J, Li Y, Han X, Yokoi K, et al. Microfluidic cytometric analysis of cancer cell transportability and invasiveness. Sci Rep 2015;5:14272.

[21] Lu JF, Bruno R, Eppler S, Novotny W, Lum B, Gaudreault J. Clinical pharmacokinetics of bevacizumab in patients with solid tumors. Cancer Chemoth Pharm 2008;62(5):779–786.

[22] Mac Gabhann F, Popel AS. Targeting neuropilin-1 to inhibit VEGF signaling in cancer: comparison of therapeutic approaches. PLoS Comput Biol 2006;2(12):e180.

[23] Manning CS, Jenkins R, Hooper S, Gerhardt H, Marais R, Adams S, et al. Intravital imaging reveals conversion between distinct tumor vascular morphologies and localized vascular response to Sunitinib. IntraVital 2013;2(1):e24790.

[24] McKenna MT, Weis JA, Barnes SL, Tyson DR, Miga MI, Quaranta V, et al. A predic-tive mathematical modeling approach for the study of doxorubicin treatment in triple negative breast cancer. Sci Rep 2017;7(1):5725.

[25] Miller JW, Adamis AP, Shima DT, D'Amore PA, Moulton RS, O'Reilly MS, et al. Vas-cular endothelial growth factor/vascular permeability factor is temporally and spatially correlated with ocular angiogenesis in a primate model. Am J Pathol 1994;145(3):574.

[26] Nilsen LB, Fangberget A, Geier O, Seierstad T. Quantitative analysis of diffusion-weighted magnetic resonance imaging in malignant breast lesions using different b value combinations. Eur Radiol 2013;23(4):1027–1033.

[27] Nilsen LB, Fangberget A, Geier OM, Engebraaten O, Borgen E, Olsen DR, et al. Associations between tumor vascularization assessed by in vivo DCE-MRI and the presence of disseminated tumor cells in bone marrow in breast cancer patients at the time of diagnosis. J Magn Reson Imaging 2014;40(6):1382–1391.

[28] Owen MR, Stamper IJ, Muthana M, Richardson GW, Dobson J, Lewis CE, et al. Mathematical modeling predicts synergistic antitumor effects of combining a macrophage-based, hypoxia-targeted gene therapy with chemotherapy. Cancer Res 2011;71(8):2826–2837.

[29] Ozawa CR, Banfi A, Glazer NL, Thurston G, Springer ML, Kraft PE, et al. Microenvironmental VEGF concentration, not total dose, determines a threshold between normal and aberrant angiogenesis. J Clin Invest 2004;113(4):516–527.

[30] Papadopoulos N, Martin J, Ruan Q, Rafique A, Rosconi MP, Shi E, et al. Binding and neutralization of vascular endothelial growth factor (VEGF) and related ligands by VEGF Trap, ranibizumab and bevacizumab. Angiogenesis 2012;15(2):171–185.

[31] Parker JS, Mullins M, Cheang MC, Leung S, Voduc D, Vickery T, et al. Supervised risk predictor of breast cancer based on intrinsic subtypes. J Clin Oncol 2009;27(8):1160–1167.

[32] Ribba B, Alarcón T, Marron K, Maini PK, Agur Z. The use of hybrid cellular automaton models for improving cancer therapy. In: International Conference on Cellular Automata Springer; 2004. p. 444–453.

[33] Royds JA, Dower SK, Qwarnstrom EE, Lewis CE. Response of tumour cells to hypoxia: role of p53 and NFkB. MP, Mol Pathol 1998 Apr;51(2):55–61.

[34] Sandström M, Freijs A, Larsson R, Nygren P, Fjällskog ML, Bergh J, et al. Lack of relationship between systemic exposure for the component drug of the fluorouracil, epirubicin, and 4-hydroxycyclophosphamide regimen in breast cancer patients. J Clin Oncol 1996;14(5):1581–1588. PMID: 8622075.

[35] Silwal-Pandit L, Nord S, von der Lippe Gythfeldt H, Møller EK, Fleischer T, Rødland E, et al. The longitudinal transcriptional response to neoadjuvant chemotherapy with and without bevacizumab in breast cancer. Clin Cancer Res 2017;p. clincanres–0160.

[36] Sugihara K, Nishiyama K, Fukuhara S, Uemura A, Arima S, Kobayashi R, et al. Autonomy and non-autonomy of angiogenic cell movements revealed by experiment-driven mathematical modeling. Cell reports 2015;13(9):1814–1827.

[37] Tannock IF. Oxygen diffusion and the distribution of cellular radiosensitivity in tumours. Brit J Radiol 1972;45(535):515–524.

[38] Tofts PS, Berkowitz B, Schnall MD. Quantitative Analysis of Dynamic Gd-DTPA Enhancement in Breast Tumors Using a Permeability Model. Magn Reson Med 1995;33(4):564–568.

[39] Yano S, Zhang Y, Miwa S, Tome Y, Hiroshima Y, Uehara F, et al. Spatial–temporal FUCCI imaging of each cell in a tumor demonstrates locational dependence of cell cycle dynamics and chemoresponsiveness. Cell Cycle 2014;13(13):2110–2119.